1.0

1.1

1.25 1.4 1.6

4.5
5.0
5.6

2.8 2.5
3.2 2.2
3.6
4.0 2.0
1.8

MICROCOPY RESOLUTION TEST CHART
NATIONAL BUREAU OF

LEVEL

DYNAMIC DATA ASSIMILATION
BY THE NOISE FREEZING METHOD

Prepared By:

Yoshi K. Sasaki, Tom Baxter, James S. Goerss

University of Oklahoma
Norman, Oklahoma 73069

SEPTEMBER 1979

DDC

DEC 11 1979

RECEIVED

A

79 12 6 128
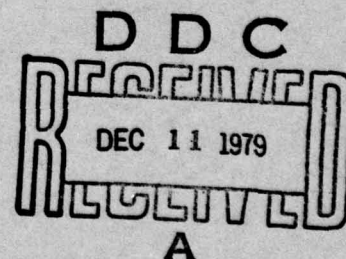
REPORT DOCUMENTATION PAGE		READ INSTRUCTIONS BEFORE COMPLETING FORM
1. REPORT NUMBER NAVENVPREDRSCHFAC Contractor Report CR-79-03	2. GOVT ACCESSION NO. NEPRF	3. RECIPIENT'S CATALOG NUMBER
4. TITLE (and Subtitle) Dynamic Data Assimilation by the Noise Freezing Method.		5. TYPE OF REPORT & PERIOD COVERED Final rept.,
		6. PERFORMING ORG. REPORT NUMBER
7. AUTHOR(s) Yoshi K. Sasaki, (principal investigator) Tom Baxter James S. Goerss		8. CONTRACT OR GRANT NUMBER(s) N00228-77-C-3056
9. PERFORMING ORGANIZATION NAME AND ADDRESS University of Oklahoma 200 Felgar Street Norman, OK 73069 F52551		10. PROGRAM ELEMENT, PROJECT, TASK AREA & WORK UNIT NUMBERS PE 62759N, PN 2F52551792 NEPRF WU 6.2-5
11. CONTROLLING OFFICE NAME AND ADDRESS Commander, Naval Air Systems Command Department of the Navy Washington, DC 20361		12. REPORT DATE September 1979
		13. NUMBER OF PAGES 80
14. MONITORING AGENCY NAME & ADDRESS(If different from Controlling Office) Naval Environmental Prediction Research Facility, Monterey, CA 93940		15. SECURITY CLASS. (of this report) UNCLASSIFIED
		15a. DECLASSIFICATION/DOWNGRADING SCHEDULE

16. DISTRIBUTION STATEMENT (of this Report)

Approved for public release; distribution unlimited.

17. DISTRIBUTION STATEMENT (of the abstract entered in Block 20, if different from Report)

18. SUPPLEMENTARY NOTES

Original manuscript received in March 1979.

19. KEY WORDS (Continue on reverse side if necessary and identify by block number)

Data assimilation
Satellite data
Numerical weather prediction

20. ABSTRACT (Continue on reverse side if necessary and identify by block number)

A barotropic model was developed using a variational method to conserve mass and total energy. This model was then used to assimilate satellite data by adjusting the fluid depth so that gravity waves moved at about the same speed as meteorological waves. The analyses resulting from the assimilation runs were used to adjust the 1000-500 mb thickness in a baroclinic forecast system. Although results were obtained from only one _____

DD FORM 1473 EDITION OF 1 NOV 68 IS OBSOLETE
S/N 0102-014-6601

20. Abstract (Continued)

experiment, they show some promise for improving forecasts, particularly in the southern hemisphere.

A baroclinic global model was then developed so that the gravity waves could be decreased in speed during the period of data assimilation of satellite data. Initial tests suggest that imbalances in the model caused by data insertion can be controlled, thereby allowing a more accurate analysis of the satellite data.

CONTENTS

i

1. INTRODUCTION

This report summarizes work in progress on the problem of assimilating satellite-derived meteorological measurements into forecast models suitable for operational use. Tests have been made with a barotropic and a baroclinic assimilation model, both employing the noise-freezing technique. For the 12-hour period between synoptic times, the assimilation model was run, taking in the satellite measurements at the time and place of observation. At the end of the 12-hour period, the forecast of the assimilation model was used to alter the first guess fields for the synoptic analysis. In this way the information gained from the satellite observations is passed along to the forecast model, unless it is vetoed by new synoptic data in the analysis scheme.

The new NEPRF global analysis and forecast system was used to test the barotropic assimilation model. Because of problems incurred when the new forecast system was prepared for operational testing, and because of limited computer availability, only one forecast was made with and without the satellite data. The results of this experiment were inconclusive, but suggest hope that improvement in the forecast might be demonstrated by continued comparisons.

1

A baroclinic assimilation model has also been tested, but a definitive evaluation has not yet been made. Results to date indicate that the limited success which was experienced with the barotropic model may be retained in the baroclinic one.

Section 2 discusses the data assimilation problem and the use of the noise freezing technique in its solution. The tests of the barotropic assimilation model with the NEPRF global forecast model are detailed in section 3, with results in section 4. Some recommendations concerning the possible application of the barotropic model are in section 5.

The baroclinic assimilation model is described in section 6, and section 7 contains a discussion of some preliminary tests.

2.   BAROTROPIC DATA ASSIMILATION

The utilization of satellite-derived temperature soundings in numerical prediction models is a problem which has defied solution, despite the efforts of many researchers. The biggest problem is that the data is distributed along the time axis, and not amenable to conventional analysis methods. One of the common methods of assimilating satellite data, referred to as updating, involves replacing the solutions in a forecast model with observed values at the time and place of the observation. In a primitive equation model, this procedure generates a great deal of gravity wave noise which, unless controlled, can easily destroy the entire forecast. If dissipative devices are used to control the noise, the quality of the forecast may suffer more from the dissipation than it is improved by the data.

Recently, the idea was suggested (Sasaki, 1976b) that the noise introduced by updating might be controlled by altering the numerical model so that the phase speeds of gravitational modes are greatly reduced. In a barotropic model, the phase speed of gravity waves depends on the square root of the mean atmospheric depth. By reducing the modelled mean depth, the gravity waves may be slowed without

3

substantially affecting the meteorologically significant waves. In a baroclinic model, the mean surface pressure plays a similar role. This technique has been referred to as the "noise freezing method" (NFM).

At a particular synoptic time, the satellite data for the previous 12-hour period would be assimilated by running the forecast model with initial data from the previous synoptic time, and updating the model solutions with the satellite data. During this assimilation period, the NFM is utilized to slow down the noise waves and reduce their interaction with the large scale. At the end of the 12-hour assimilation period, the noise which has accumulated must be removed, the conventional data incorporated, and the forecast model is then initialized with the resulting fields.

2.1 MODEL DESCRIPTION

A global barotropic primitive equation forecast model with variational energy and mass conservation was the assimilation forecast vehicle in the study. The variational conservation algorithm is especially beneficial in the assimilation experiments to prevent instabilities.

The model equations are:

$$\frac{\partial (hu)}{\partial t} + \frac{1}{a \cos \theta} \left[\frac{\partial}{\partial \lambda} (huu) + \frac{\partial}{\partial \theta}(hvv \cos \theta) \right] - hv \left(f + \frac{u \tan \theta}{a}\right)$$
$$+ \frac{g}{a \cos\theta} h \frac{\partial h}{\partial} = 0 \tag{1}$$

4

$$\frac{\partial (hv)}{\partial t} + \frac{1}{a \cos \theta} \left[\frac{\partial}{\partial \lambda} (huv) + \frac{\partial}{\partial \theta} (hvv \cos \theta) \right] + hu \left(f + \frac{u \tan \theta}{a} \right)$$

$$+ \frac{g}{a} h \frac{\partial h}{\partial \theta} = 0 \tag{2}$$

$$\frac{\partial h}{\partial t} + \frac{1}{a \cos \theta} \left[\frac{\partial (hu)}{\partial \theta} + \frac{\partial}{\partial \theta} (hv \cos \theta) \right] = 0 \tag{3}$$

where a is the radius of the earth, g is the acceleration of gravity, h is depth of the layer, u is the eastward wind component, v is the northward wind component, t is time, λ is longitude, θ is latitude, and f is the coriolis parameter (= $2\Omega \sin \theta$, Ω is the angular velocity of the earth).

The model conserves the total mass and the total energy:

$$\int_{-\pi}^{\pi} \int_{0}^{2\pi} h \, a^2 \cos \theta \, d\lambda \, d\theta = <h> \tag{4}$$

and

$$\int_{-\pi}^{\pi} \int_{0}^{2\pi} \left[\frac{h}{2} (u^2 + v^2) + \frac{g}{2} h^2 \right] a^2 \cos \theta \, d\lambda \, d\theta = <T> \tag{5}$$

where $<h>$ and $<T>$ are constants determined from the initial fields.

5

2.2 VARIATIONAL CONSERVATION SCHEME

A variational finite difference method (Sasaki, 1976a) is used to solve the prognostic equations (1) ~ (3) under the constraints (4) ~ (5). To save computer time, an equal-area longitude-latitude grid system is used to mesh the global surface. The variables h, u, v are assigned at each grid point.

The variationally designed scheme requires the following steps: (i) One time step forecasting of all the variables by arbitrarily selected finite difference form of (1) ~ (3) (the Leap-frog-flux form is chosen in this experiment). These forecasts are written $\tilde{h}$, $\tilde{u}$ and $\tilde{v}$; (ii) Adjusting $\tilde{h}$, $\tilde{u}$ and $\tilde{v}$ to satisfy the conservation equations (4) ~ (5). This is done by forcing the first variation of a functional to vanish, i.e.:

$$\delta J = \delta \left\{ \Sigma \left[\tilde{\alpha} (u-\tilde{u})^2 + \alpha (v-\tilde{v})^2 + \beta (h-\tilde{h})^2 \right] \right.$$
$$\left. + \lambda_E \left[\Sigma \left(\frac{h}{2} (u^2 + v^2) + \frac{g}{2} h^2\right) - T^0 \right] + \lambda_M \left[\Sigma h - h^0 \right] \right\} = 0$$

$$(6)$$

where δ is the first variational operator, J is the functional, Σ is a sum over all grid points, $\tilde{\alpha}$ and $\tilde{\beta}$ are constant weights, T^0 is the sum of total energy over all grid points at $t = 0$, h^0 is the sum of depth over the entire grid at $t = 0$, λ_E and λ_M are the Lagrange multipliers for total energy and total mass conservation, respectively. The numerical method for solving Eq. (6) is described in

6

Sasaki (1976a). Some numerical values are $\Delta t = 5$ min.,
$\Delta \theta = 5°$ in longitude, $\Delta \theta = 3.2°$ in latitude near the equator,
increasing at higher latitudes in such a way that the area
of all grid elements is constant.

2.3 NOISE FREEZING TECHNIQUE

Since the satellite data have sizable errors, con-
siderable noise may result from their use in updating a fore-
cast model. It seems highly desirable to prevent the noise
which results from such errors from spreading so rapidly.
However, we need to ensure that the waves of meteorological
importance are not affected.

The basic idea of the experiment conducted to achieve
the above objectives will be illustrated. Let us consider
for simplicity a linear set of equations with the assumption
that $\partial / \partial y = 0$ except for the coriolis parameter f on a local
cartesian coordinate system (x,y), which corresponds to the
complete form (1) ~ (3):

$$\frac{\partial u}{\partial t} + U \frac{\partial u}{\partial x} - fv = -g \frac{\partial h}{\partial x} \tag{7}$$

$$\frac{\partial v}{\partial t} + U \frac{\partial v}{\partial x} + fu = 0 \tag{8}$$

$$\frac{\partial h}{\partial t} + U \frac{\partial h}{\partial x} = -\gamma H \frac{\partial u}{\partial x} \tag{9}$$

where U is the mean zonal current velocity, H is the mean
depth of the layer and $\gamma = 1$ (nondimensional constant). The
corresponding nondimensional equations are

7

$$R_0 \left(\frac{\partial u'}{\partial t'} + U' \frac{\partial u'}{\partial x'}\right) - fv' = -\frac{\partial h'}{\partial x'} \tag{10}$$

$$R_0 \left(\frac{\partial v'}{\partial t'} + U' \frac{\partial v'}{\partial x'}\right) + fu' = 0 \tag{11}$$

$$\varepsilon \left(\frac{\partial h'}{\partial t'} + U' \frac{\partial h'}{\partial x'}\right) = -\gamma \frac{\partial u'}{\partial x'} \tag{12}$$

where the primed quantities are nondimensional and the follow-
ing quantities with asterisks are dimensional: $u = v*v'$,
$U = v*U'$, $h = h*h'$, $f = f*f'$, $x = x*x'$, $t = t*t'$; R_0 is the
Rossby number $(v*/f*x*)$ and $\varepsilon = h*/H$. For meteorological
motion, the following relations are assumed:

$$t* = x*/v* \qquad \text{and} \qquad \frac{gh*}{f* \, x* \, v*} = 1$$

For global motion, R_0 ranges from about 0.1 in mid-latitudes
to about 1.0 in the tropics. However, $\varepsilon \sim 10^{-2}$ since $h* \sim$
$10^2 m$, $H \sim 10^4$ m. Therefore, the solutions are expanded
about the small parameter ε:

$$h' = \varepsilon^0 h_0' + \varepsilon^1 h_1' + \varepsilon^2 h_2' + \dots$$

$$u' = \varepsilon^0 u_0' + \varepsilon^1 u_1' + \varepsilon^2 u_2' + \dots$$

$$v' = \varepsilon^0 v_0' + \varepsilon^1 v_1' + \varepsilon^2 v_2' + \dots \tag{13}$$

For ε^0, we obtain the same equations as (10) and (11) except
that $u' \rightarrow u_0'$, $v' \rightarrow v_0'$, and $h' \rightarrow h_0'$, and (12) is simply
reduced to $\partial u_0'/\partial x' = 0$. This means that the meteorological
motion is primarily rotational. The vorticity equation is

8

obtained by cross differentiation of (10) and (11),

$$R_O \left(\frac{\partial \xi'}{\partial t'} + U' \frac{\partial \xi'}{\partial x'}\right) - \beta' v' - f' \frac{\partial u'}{\partial x'} = 0 \qquad (14)$$

where $\xi' = \partial v'/\partial x'$ and $\beta' = \partial f'/\partial y'$. Elimination of $\partial u'/\partial x'$ from (12) and (14) leads to an equation equivalent to the potential vorticity equation:

$$\gamma \ R_O \left(\frac{\partial \xi'}{\partial t'} + U' \frac{\partial \xi'}{\partial t'}\right) - \beta' v' + \epsilon f' \left(\frac{\partial h'}{\partial t'} + U' \frac{\partial h'}{\partial x'}\right) = 0 \qquad (15)$$

Since $\epsilon \sim 10^{-2}$ and $\gamma = 1$, the vorticity equation of meteorological significance is obtained by omitting the terms multiplying ϵ,

$$R_O \left(\frac{\partial \xi_O'}{\partial t'} + U' \frac{\partial \xi_O'}{\partial x'}\right) - \beta' v_O' = 0 \qquad (16)$$

Suppose we now arbitrarily adjust the value of γ. As long as γ is between 1.0 and 0.1, the same result as (16) will be obtained from (15). Since the phase velocity of the inertial external gravity waves is $U \pm \sqrt{\gamma g H + f^2/k^2 m}$ any choice of a value of γ between 1.0 and 0.1 would result in slowing down the noise wave phase velocity without materially altering the motion of meteorological significance.

This statement must be qualified for long waves. Reducing γ in (9) decreases the effect of the divergence on height changes. As was shown by Cressman (1959), the correct specification of the phase speeds of long waves relies on the inclusion of the divergence. If γ is reduced, we may expect the long waves to move more slowly.

9

3.   TEST WITH NEPRF GLOBAL MODEL

Since previous experiments with the barotropic
noise-freezing model produced better forecasts with the
satellite data than without it, we decided to test the
scheme in combination with the new NEPRF global model.
Programs were prepared to fit within the framework of the
semi-operational global model.

At each synoptic time, the barotropic assimilation
model is initialized at the previous synoptic time, using
the 500 mb analyses for that time, which are already avail-
able. The assimilation model makes a 12-hour forecast,
absorbing the satellite observations at the proper time and
place. A Cressman weighting function was used to spread the
influence of each observation over a 3-grid interval radius.

$$WT = \frac{3^2 - D^2}{3^2 + D^2}$$

where D is the distance in grid intervals between the grid
point and the observation.

Only the 1000-500 mb thickness was used from each
satellite sounding. The height of the 1000 mb surface,
interpolated in time and space from the operational analyses,
was added to the thickness to obtain a 500 mb height.

10

The resulting 12-hour forecast of the 500 mb height was used to alter the first guess fields for the geopotential analyses at the next synoptic time. First, the 500 mb height forecast was converted to a 1000-500 mb thickness by subtracting the 1000 mb height from the first guess fields. For this experiment these first guess fields were the FNWC operational analyses. In an operational situation, they would be the 12-hour forecast of the global NEPRF model.

Next, the 1000-500 mb thickness forecasted by the assimilation model was hydrostatically converted to a mean temperature. Then the 1000-500 mb mean temperature of the first guess was computed and subtracted from the mean temperature forecasted by the assimilation model. This temperature correction was applied at every pressure level, and corrected first guess geopotentials were computed hydrostatically. The temperature fields were not corrected.

The corrected first guess fields were then used by the analysis programs to generate the initial fields for the forecast. Of course the new synoptic data will overrule any discrepancy with the first guess.

So far only one case has been run to evaluate the impact of the satellite data assimilation. Problems associated with the semi-operational implementation of the NEPRF model have prevented further progress. The results of this test are discussed in the next section.

11

4. RESULTS OF TEST

The data from 1200Z July 16, 1978 was selected at
random to test the effect of the assimilation scheme on the
operational forecast. Figure 1 is the 12-hr. forecast made
by the barotropic assimilation model, incorporating the
satellite measurements as indicated in the figure. This 500
mb field was used to alter the first guess fields for the
1200Z analysis as discussed above. Figure 2 is the resulting
500 mb D-value analysis for 1200Z, and should be compared to
Figure 3, the analysis for the same time without the influ-
ence of the satellite data.

There are several notable differences between Figures
2 and 3. The most striking effect is the low on the east
coast of Argentina which is absent in the analysis without
satellite data. A D-value report of -280 m at Bahia Blanca,
Argentina was rejected by the routine analysis procedure,
but was accepted when the first guess was altered by the
assimilation forecast; a cyclone did develop in that area.
The Aleutian low was deepened by about 80 m by the influence
of the satellite data, while the low off the west coast of
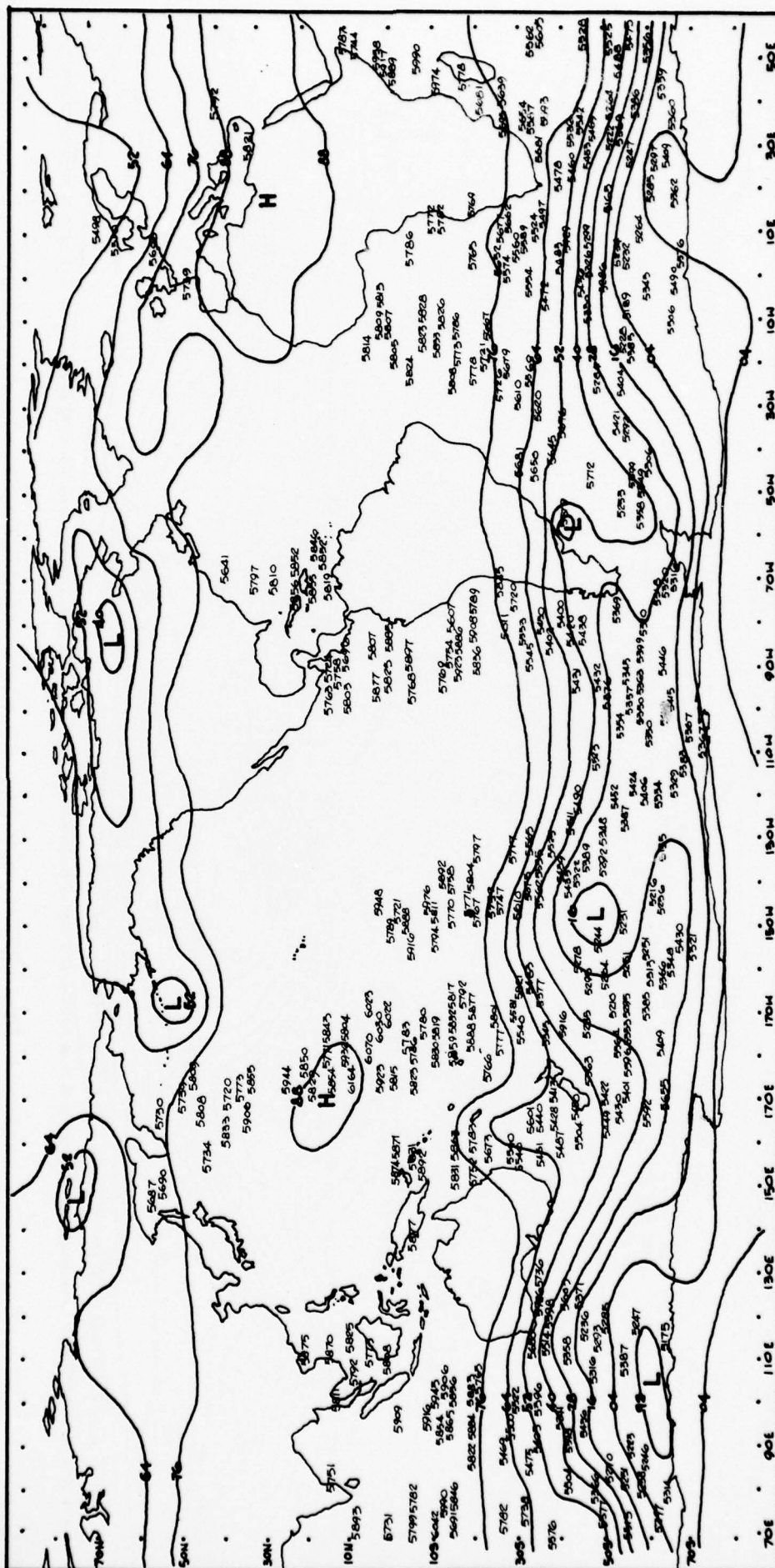Spain was filled by 20 m. In the Southern Hemisphere the

12

Figure 1. 12-HR Assimilation Forecast for 12Z 16 Jul78 500 mb HT with satellite reports.

13

Figure 2. 500 mb D-value analysis for 1200Z July 16, 78 with satellite data assimilation.
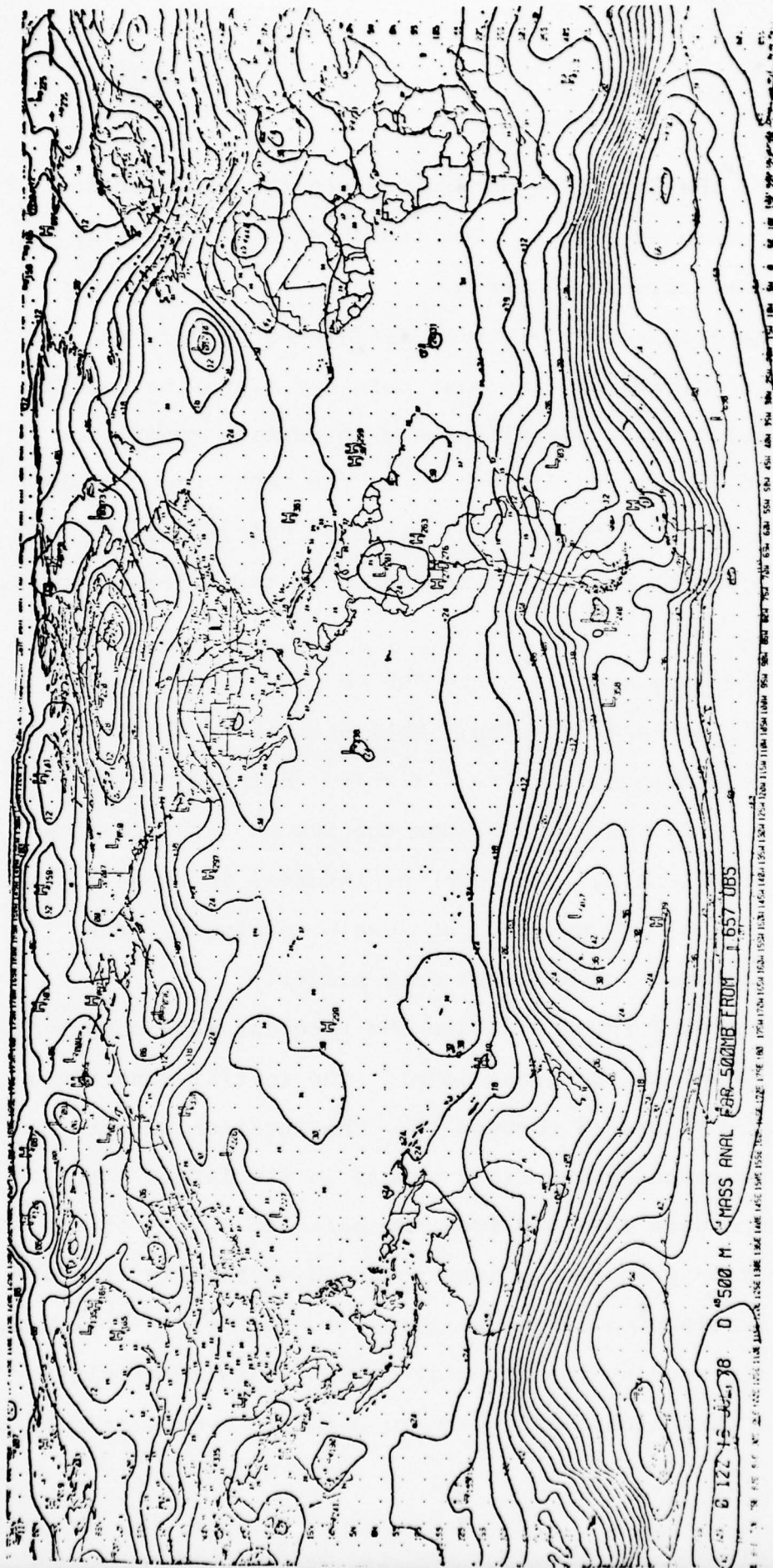
Figure 3.   500 mb D-value analysis for 1200Z July 16, 78 without satellite data.

15

addition of the satellite data decreased the geopotential gradients south of Africa. The trough east of Australia is more pronounced in Figure 2.

The only really striking difference between the two analyses is the low off the east coast of Argentina. It is to be expected that this difference in initial conditions should lead to a large difference in the NEPRF model forecasts made from the two initial states. Unfortunately, this difference almost entirely disappeared in the forecast model, as we shall see.

Figures 4 and 5 are the 500 mb temperature analyses with and without assimilation. Notice that the Argentine low is more prominent with assimilation, but also exists without it. Figures 6 and 7 show the 500 mb D-values after variational balancing. The contour interval in these figures is twice the one in the previous D-value analyses. The balancing altered the analyses only slightly.

Figures 8 through 31 are the forecast maps output by the NEPRF global forecast model. The initial conditions are given by Figures 8 through 15. The duration of the forecast is given by the first number in the label. The initial maps were obtained from the balanced output of the initialization programs by interpolating vertically from the pressure levels used in the analyses to the terrain-following sigma levels used by the forecast model. This interpolation involves a variational algorithm to maintain hydrostatic balance.
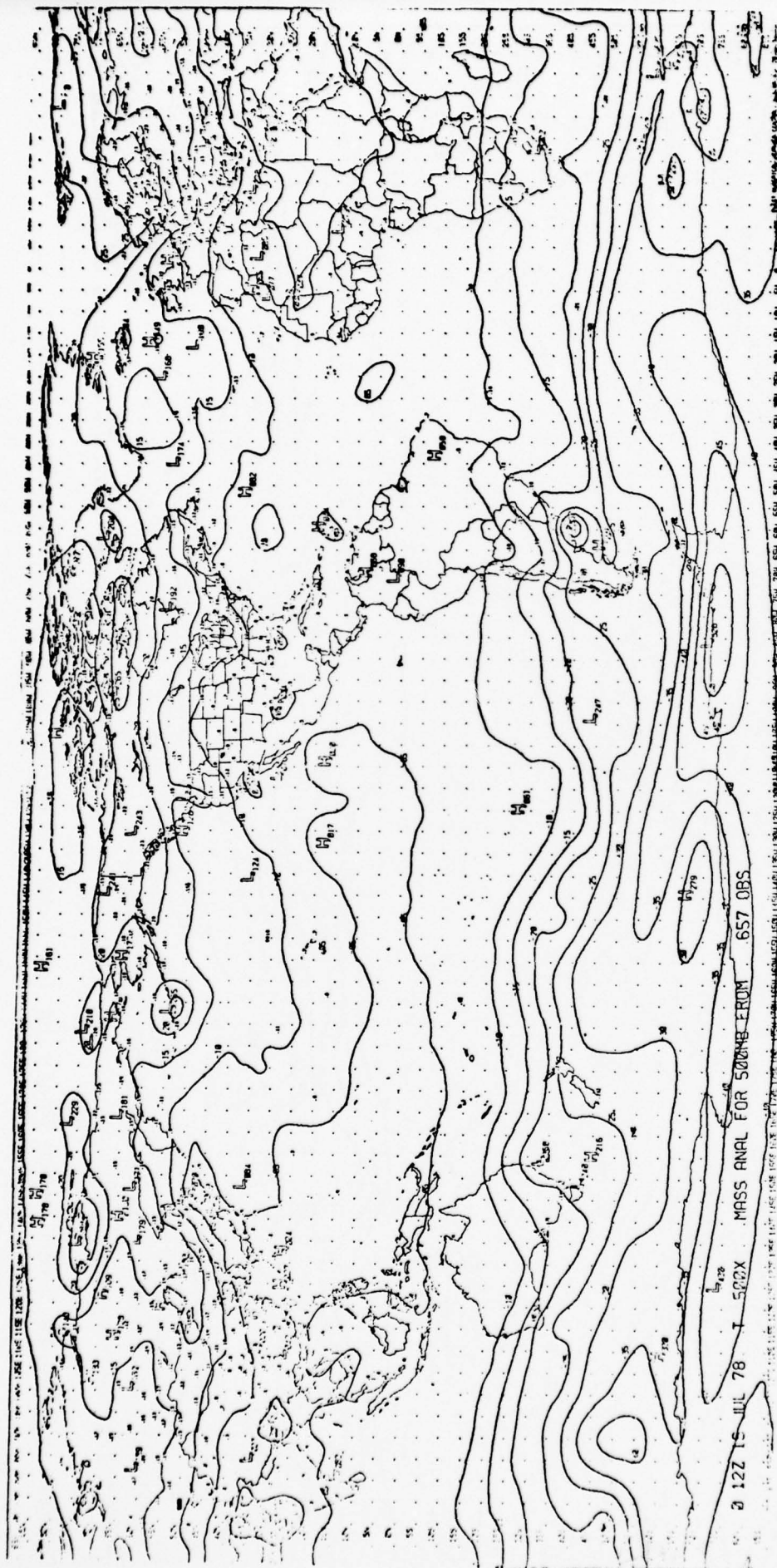
16

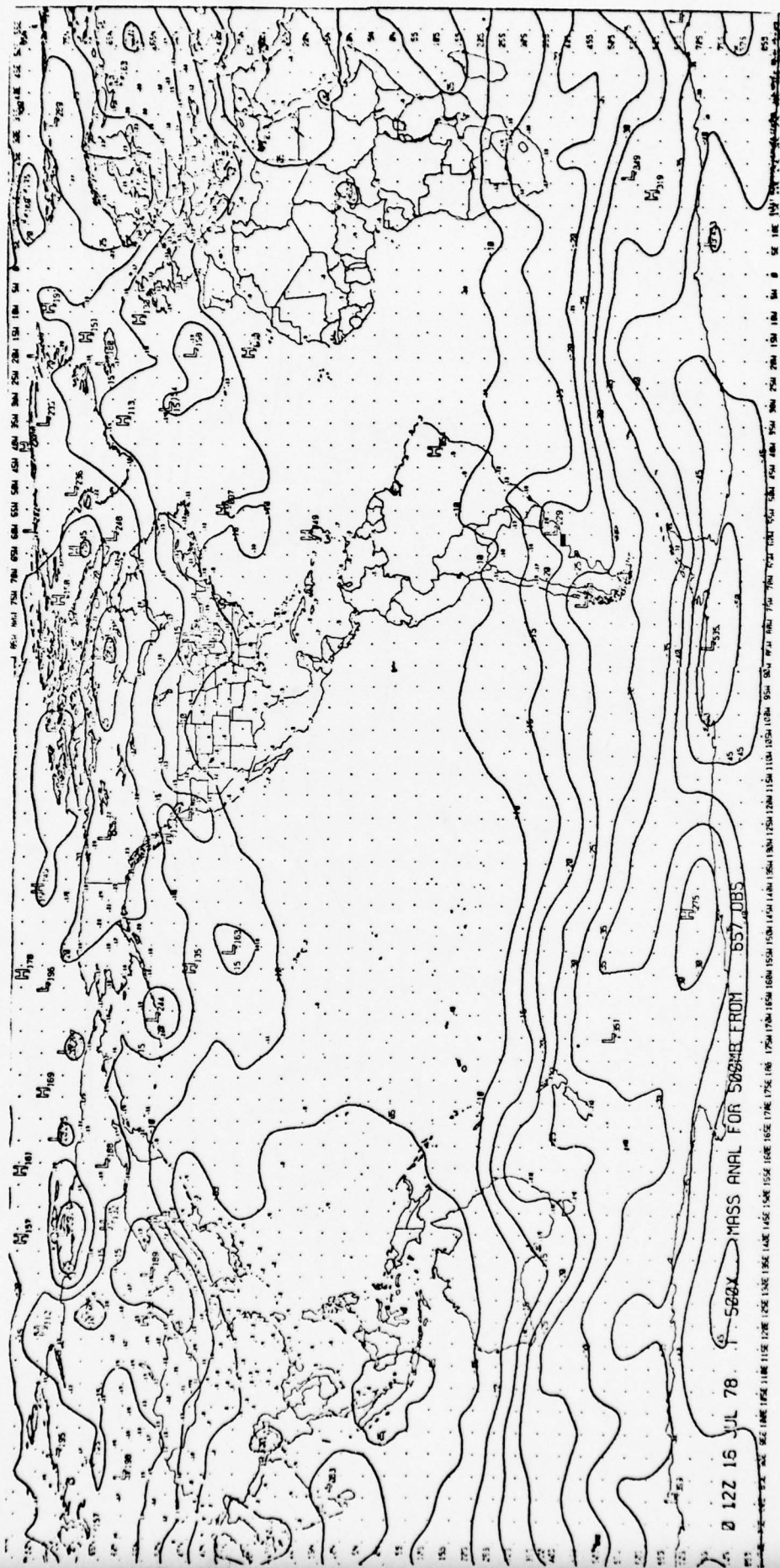Figure 4.   500 mb Temperature Analysis for 1200Z July 16, 78 with Satellite Data.

17

Figure 5. 500 mb Temperature Analysis for 1200Z July 16, 78 Without Satellite Data.

18
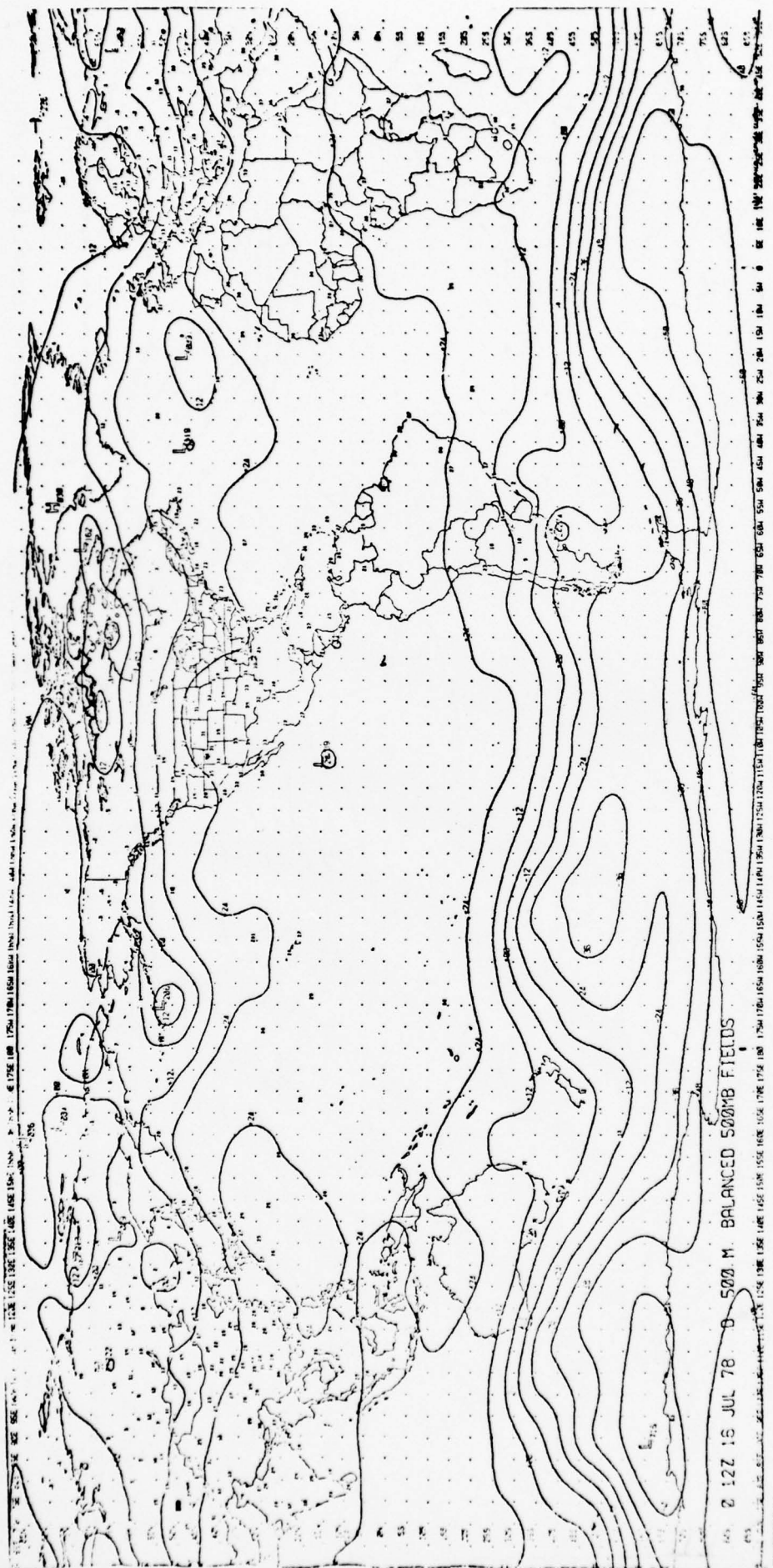
Figure 6. 500 mb D-Value After Variational Balancing for 1200Z July 16, 78 with Assimilation.

19

0 12Z 16 JUL 78. D . 500 M. BALANCED 500MB FIELDS
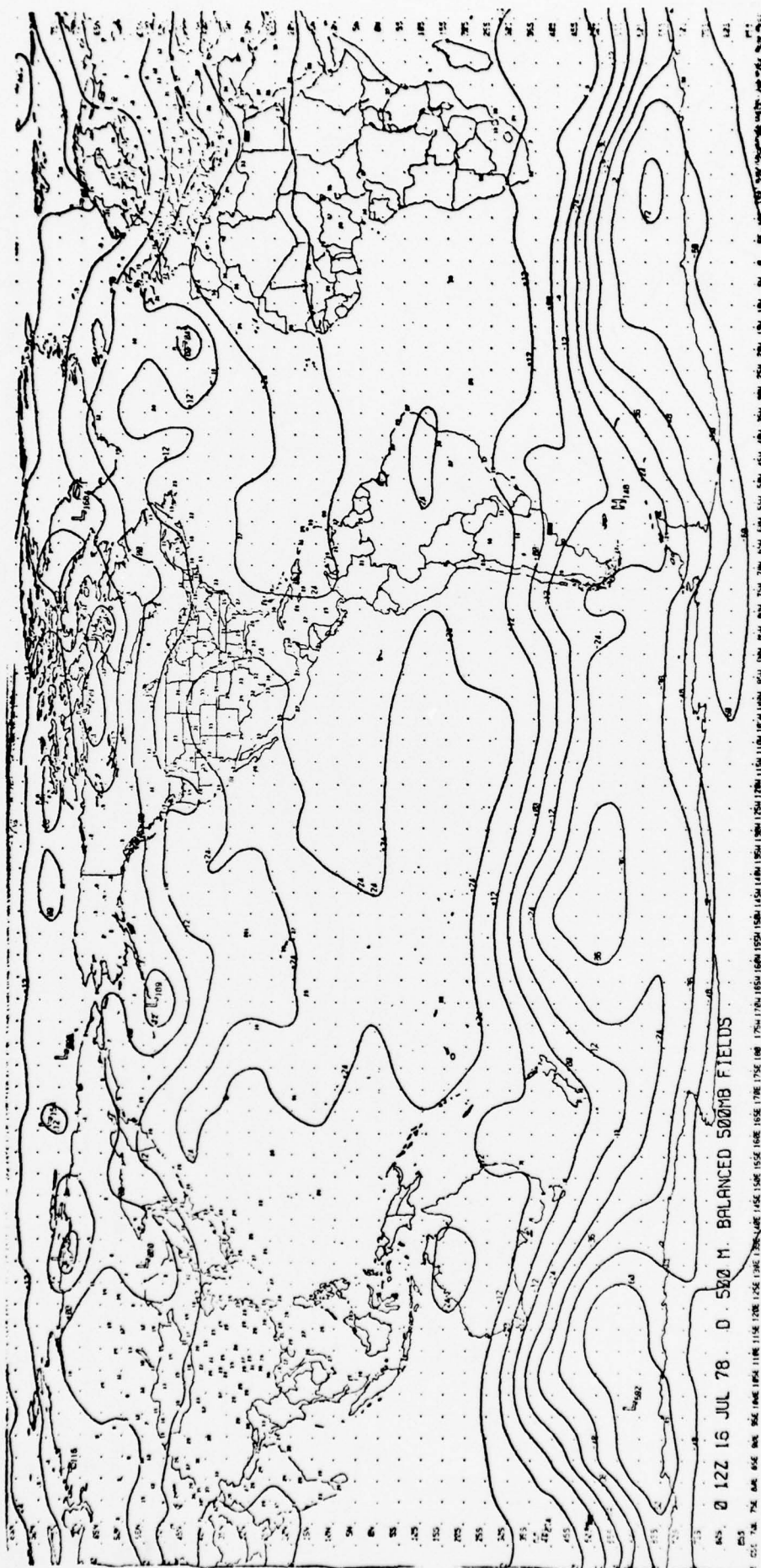
Figure 7. 500 mb D-Value After Variational Balancing for 1200Z July 16, 78 Without Satellite Data.

20

Figure 8. 500 mb Geopotential Height for N. Hem. for initial time from
NEPRF Global Model.

With Assimilation

21

0 12Z 16 JUL 78   D 500 M GEOPOTENTIAL AT 500 MBS - NEPRF/UCLA
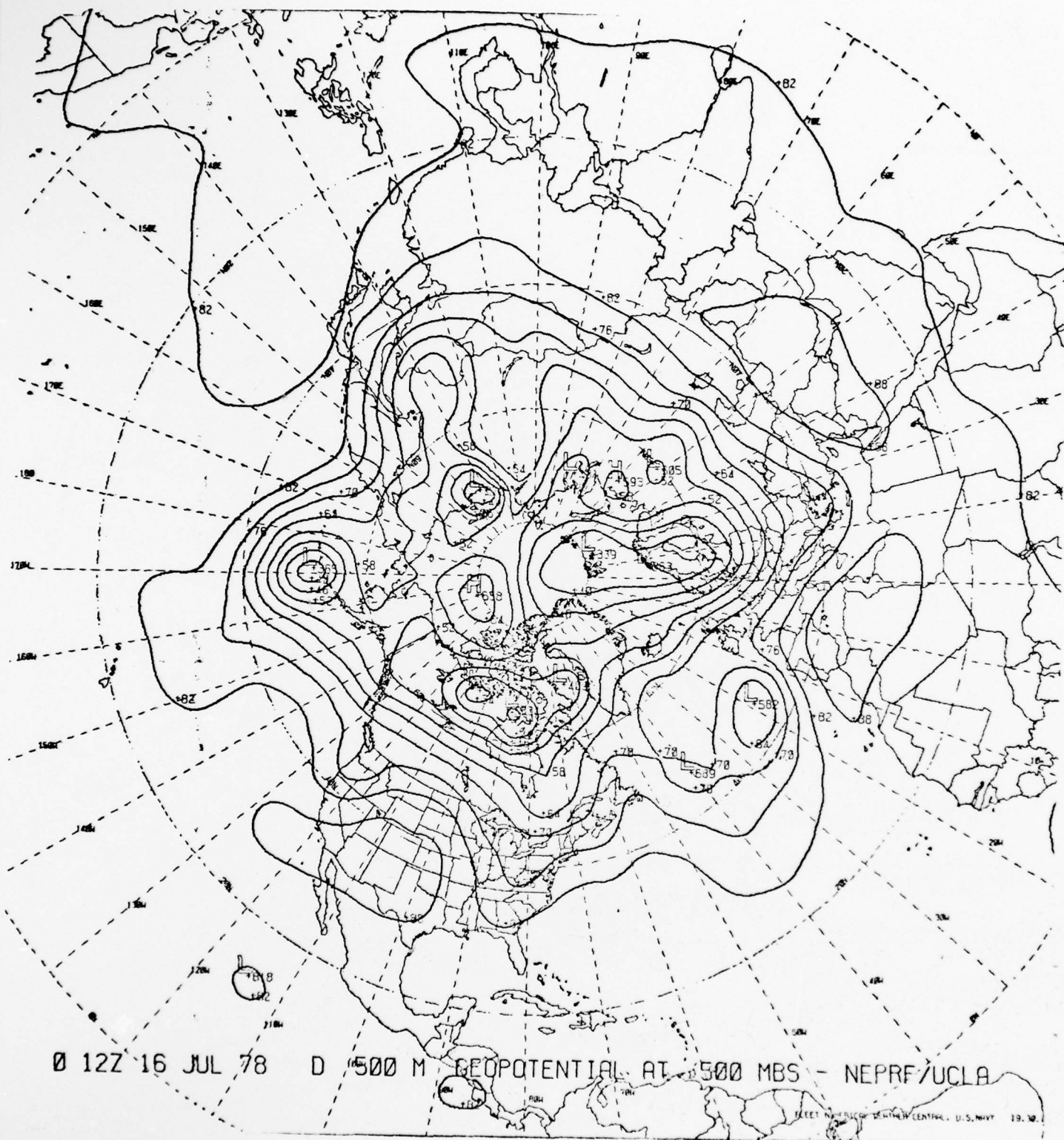
Figure 9.   500 mb Geopotential Height for N. Hem. for initial time from
NEPRF Global Model.

Without Assimilation

22

Ø 12Z 16 JUL 78 = Ø 500 M GEOPOTENTIAL AT 500 MBS - NEPRF/UCLA

Figure 10.   500 mb Geopotential Height for S. Hem. for initial time from
NEPRF Global Model.

With Assimilation

23
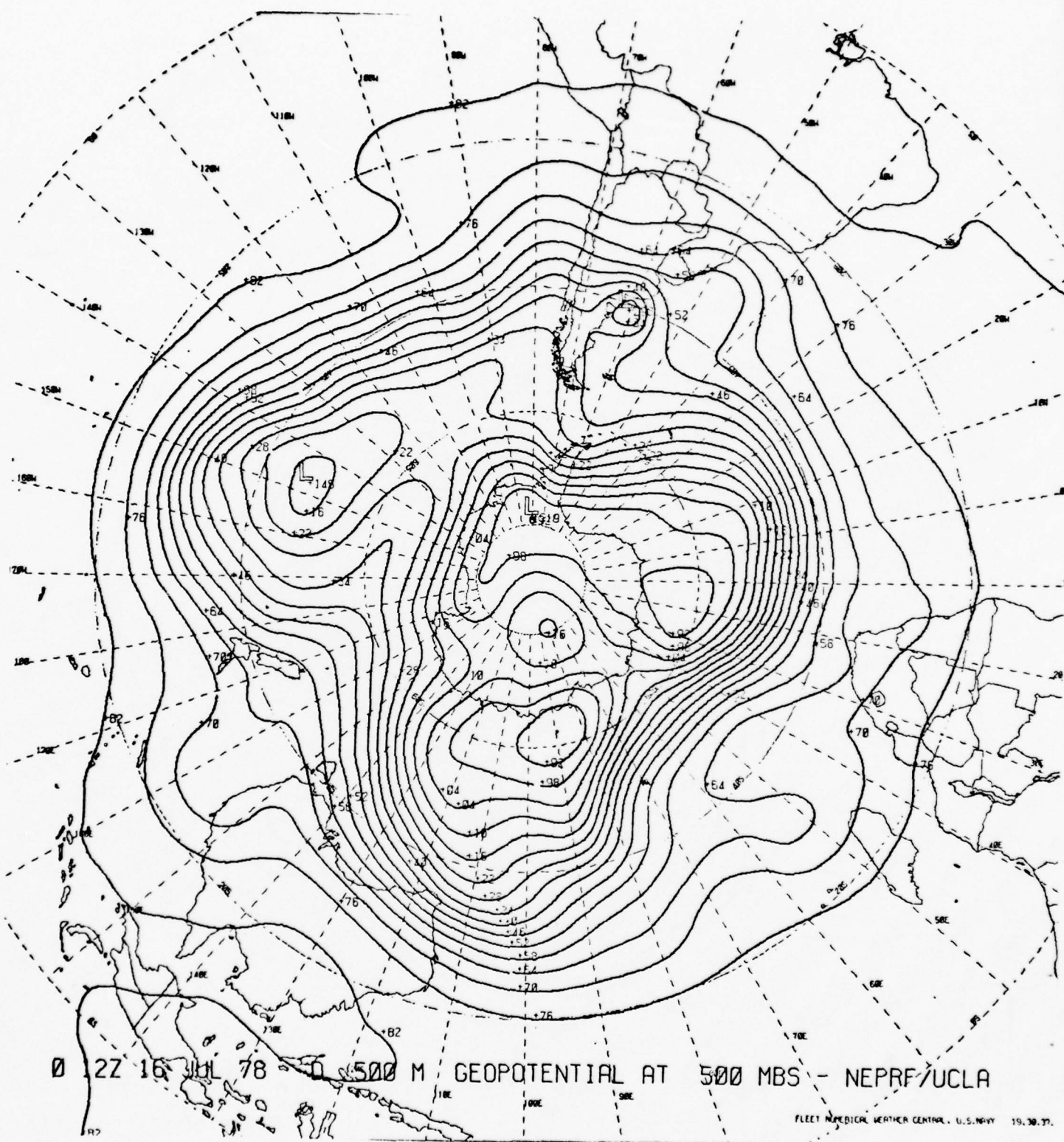
Figure 11. 500 mb Geopotential Height for S. Hem. for initial time from NEPRF Global Model.
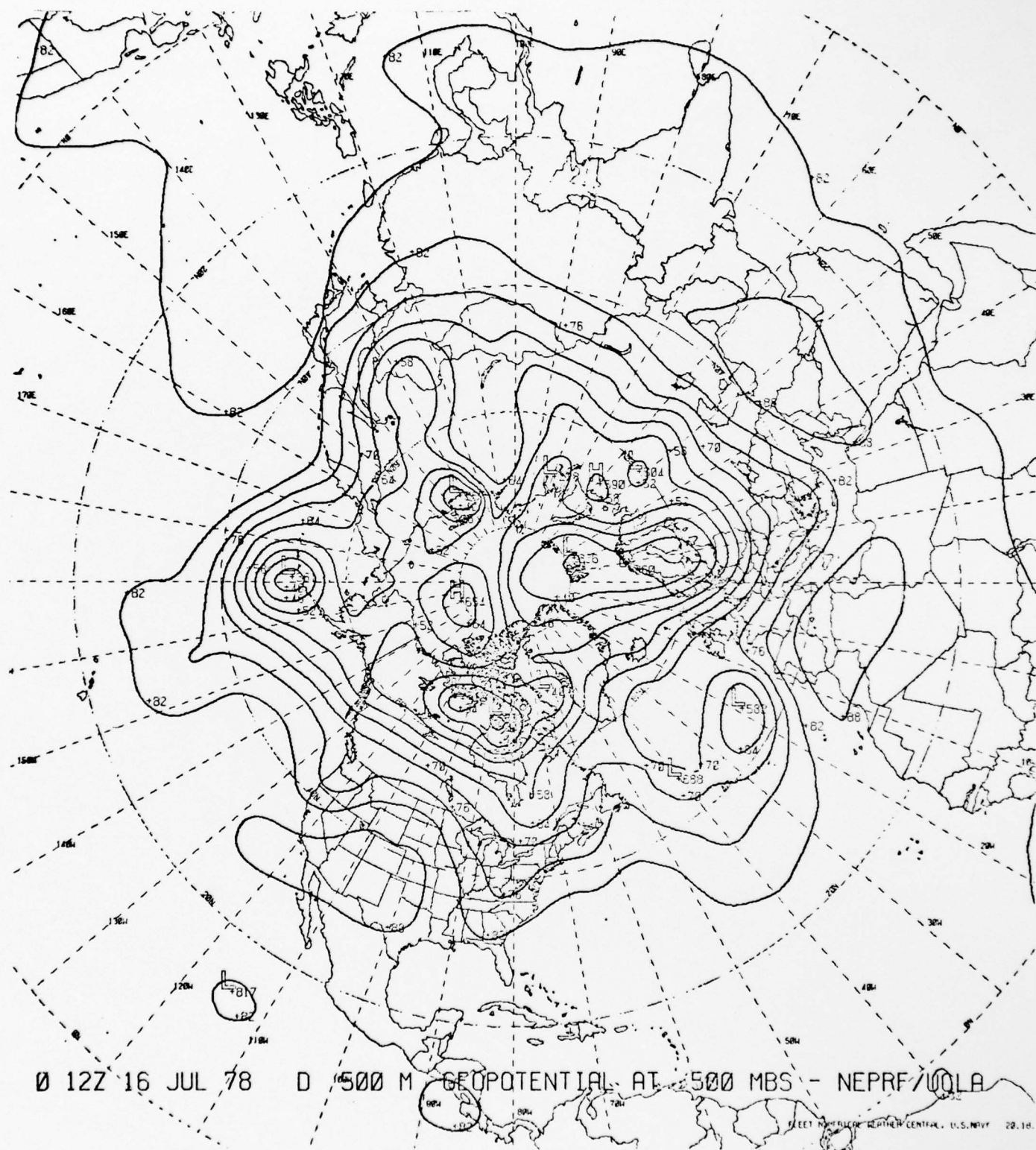
Without Assimilation

24

Ø 12Z 16 JUL 78   PS   SEA LEVEL PRESSURE - NEPRF/UCLA
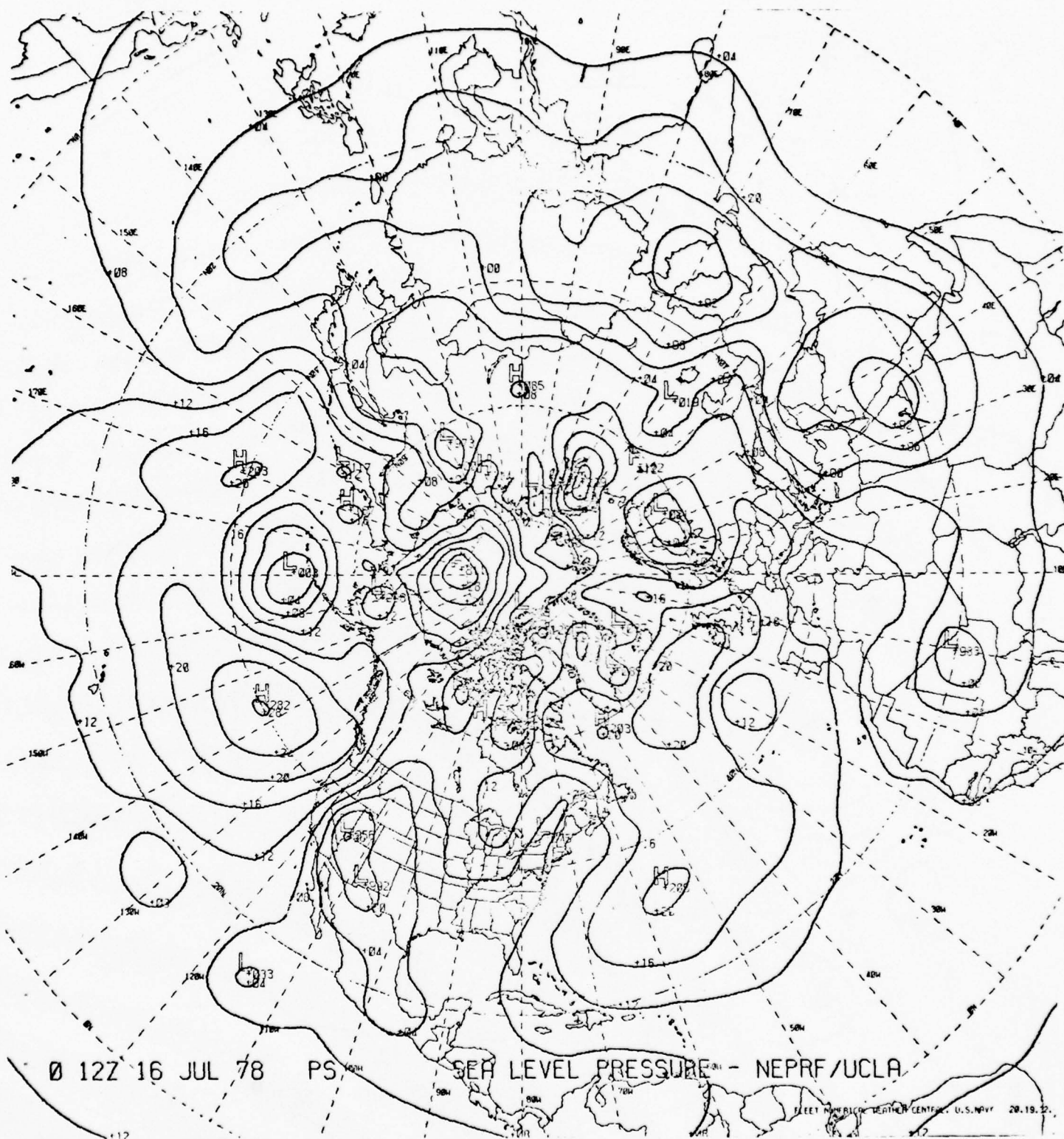
Figure 12.   Sea Level Pressure for N. Hem. for initial time from NEPRF
              Global Model.

With Assimilation

25
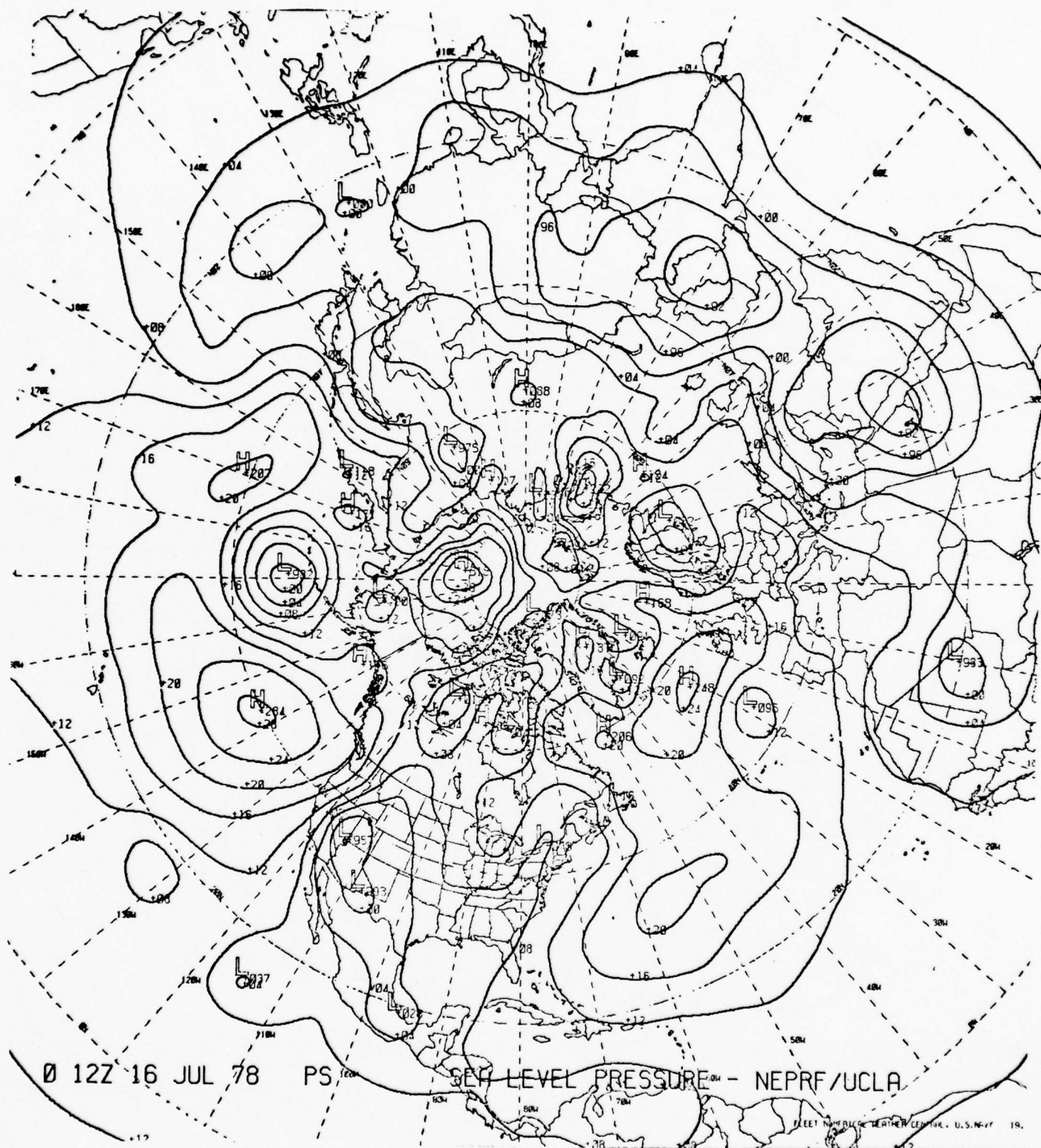
Figure 13. Sea Level Pressure for N. Hem. for initial time from NEPRF Global Model.

Without Assimilation

26
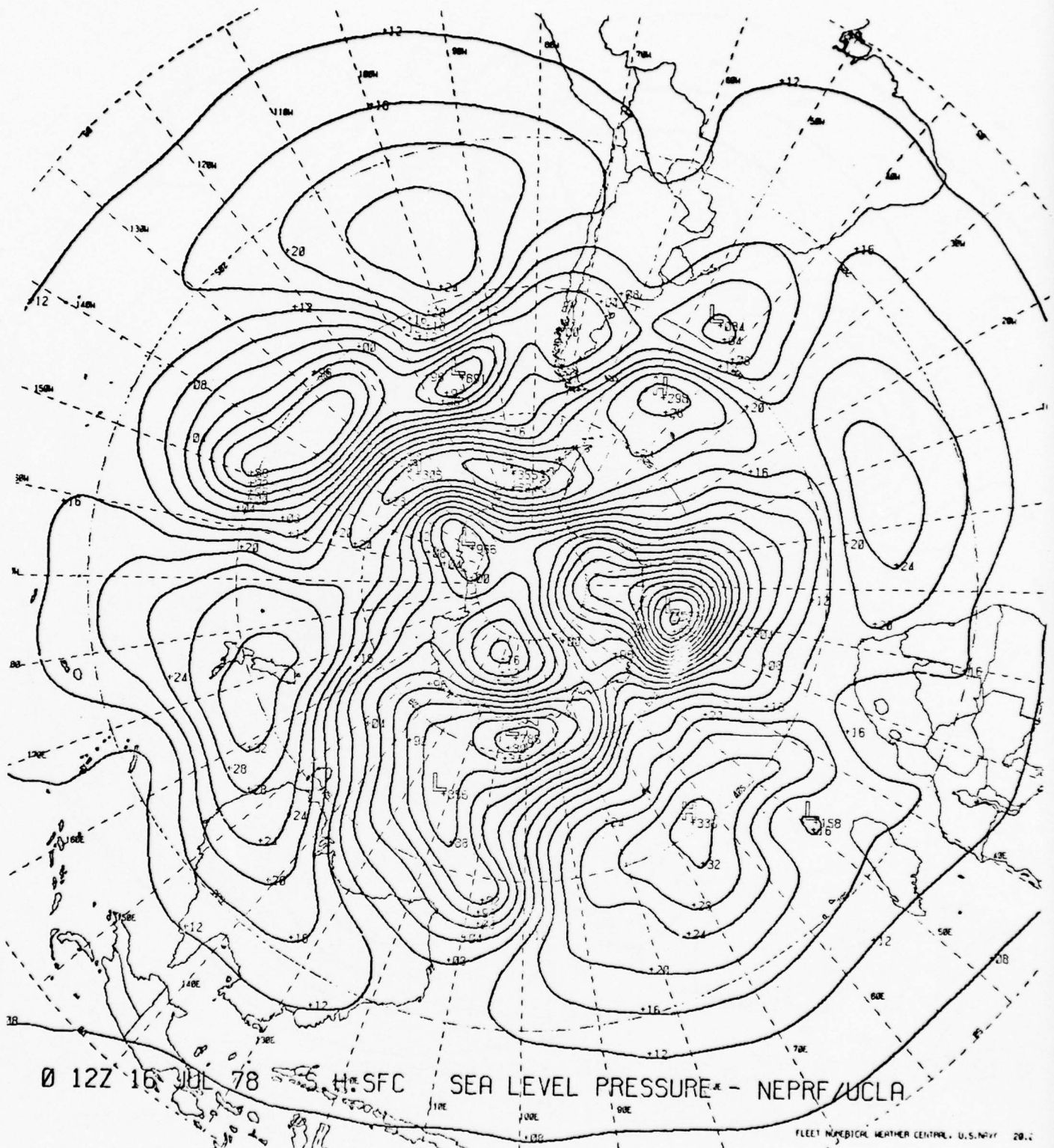
Figure 14. Sea Level Pressure for S. Hem. for initial time from NEPRF Global Model.

With Assimilation

27
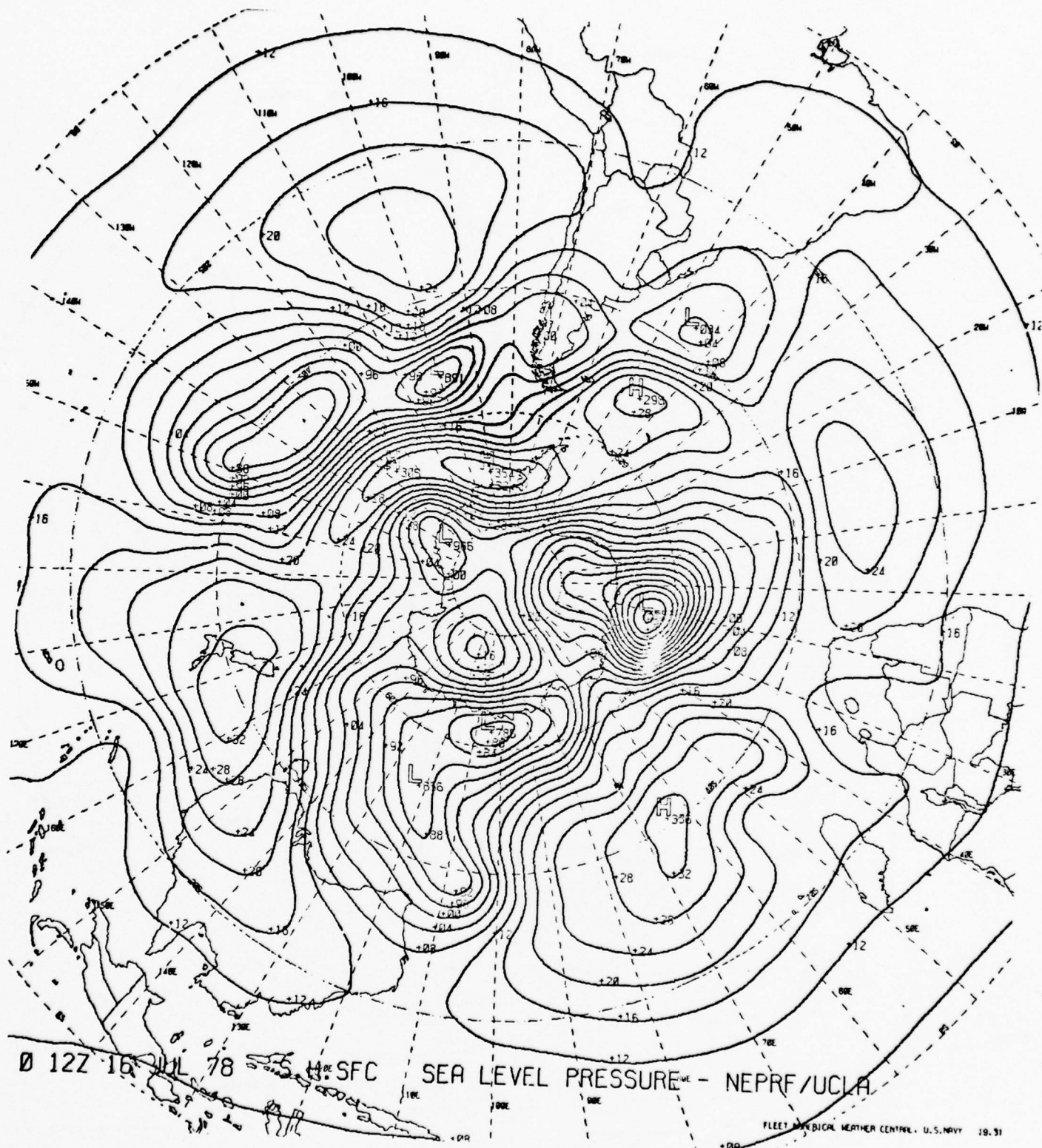
Figure 15. Sea Level Pressure for S. Hem. for initial time from NEPRF
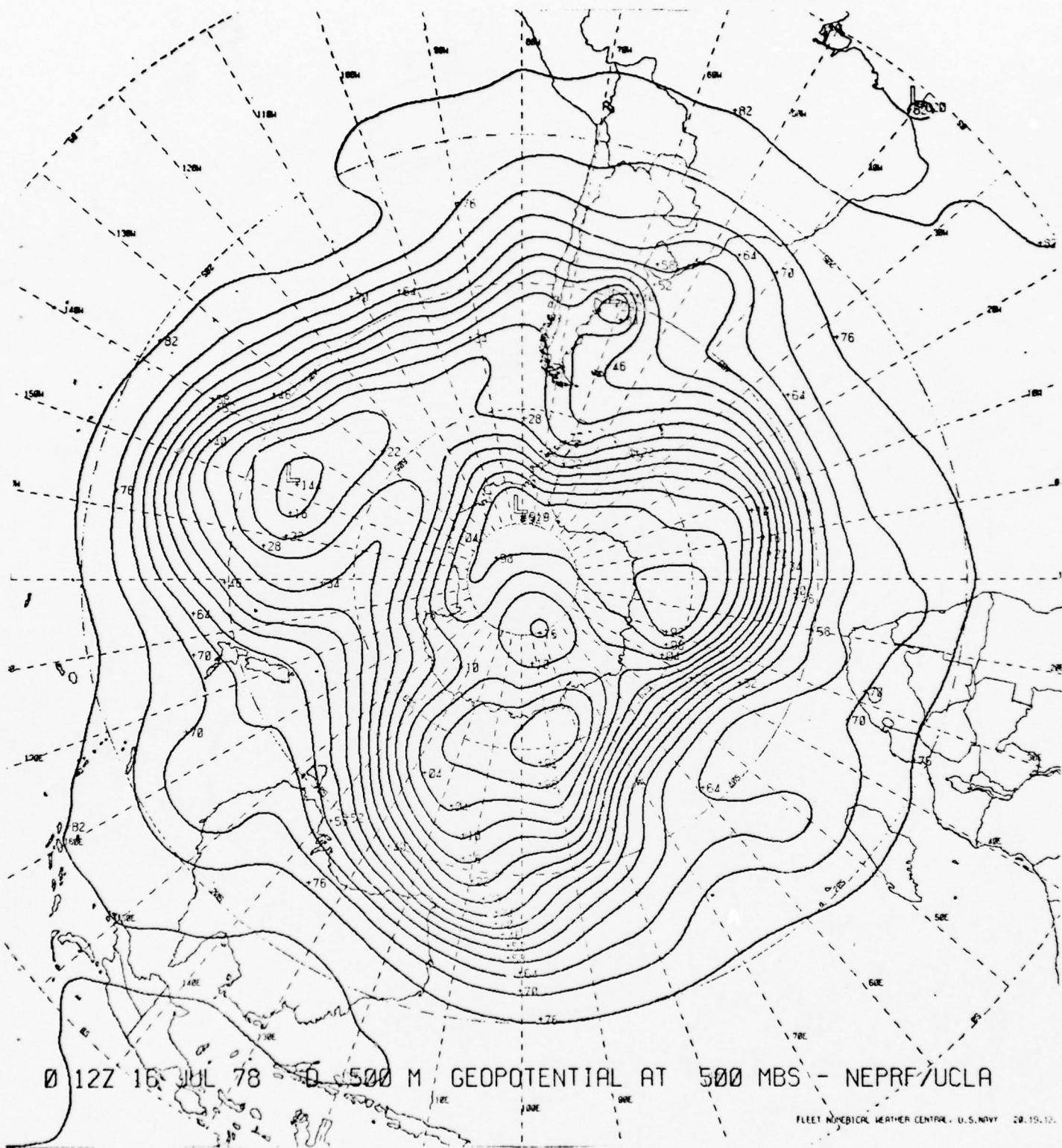Global Model.

Without Assimilation

28

24 12Z 16 JUL 78   D 500 M GEOPOTENTIAL AT 500 MBS - NEPRF/UCLA

Figure 16.   24-hr. Forecast 500 mb Geopotential Height for N. Hem.

With Assimilation

29

24 12Z 16 JUL 78   D 500 M GEOPOTENTIAL AT 500 MBS - NEPRF/UCLA

Figure 17.   24-hr. Forecast 500 mb Geopotential Height for N. Hem.

Without Assimilation

30

24 12Z 16 JUL 78   D 500 M GEOPOTENTIAL AT 500 MBS - NEPRF/UCLA

Figure 18.   24-hr. Forecast 500 mb Geopotential Height for S. Hem.

With Assimilation

31
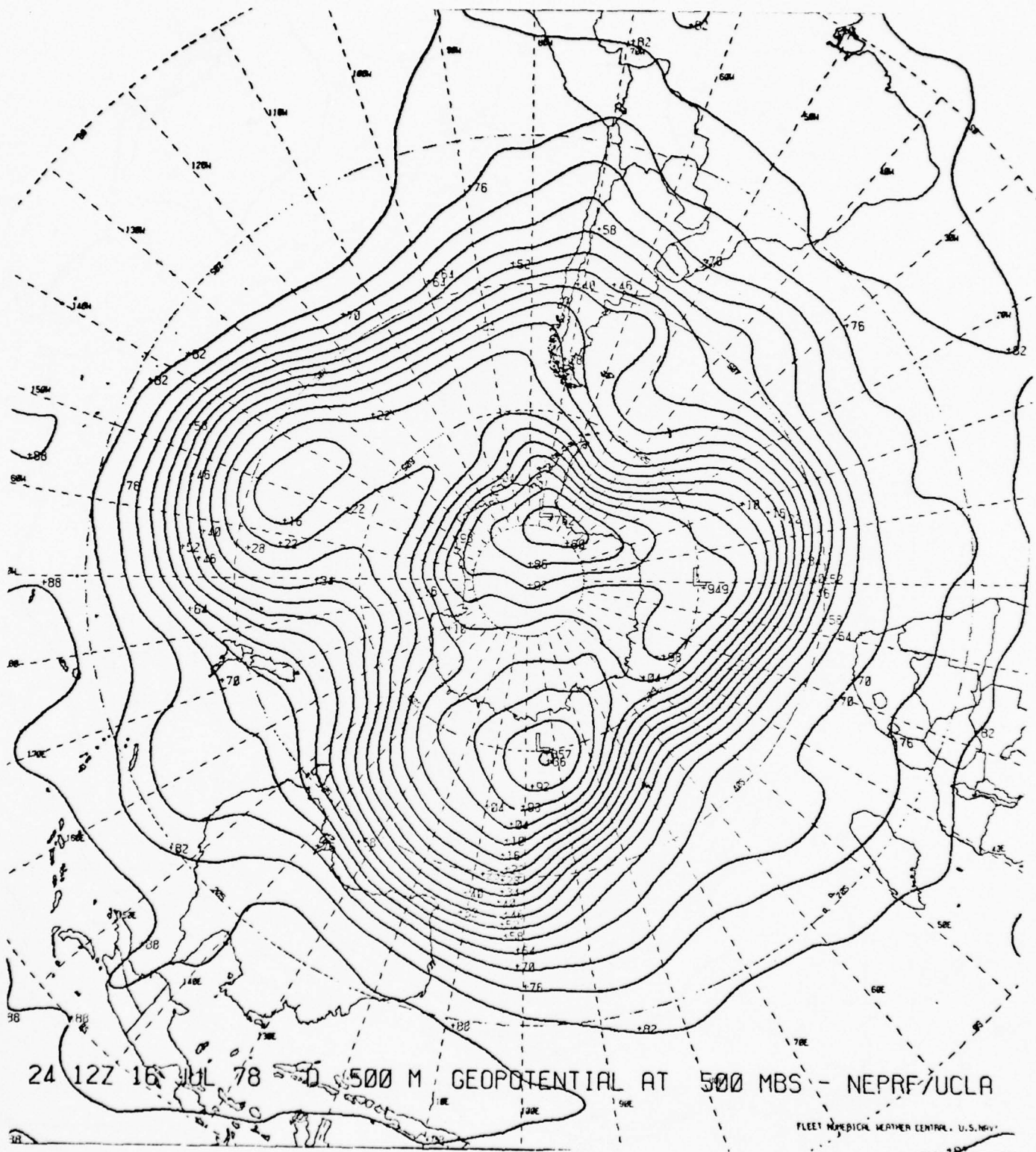
Figure 19.   24-hr. Forecast 500 mb Geopotential Height for S. Hem.

Without Assimilation

32

24 12Z 16 JUL 78   PS   SEA LEVEL PRESSURE - NEPRF/UCLA
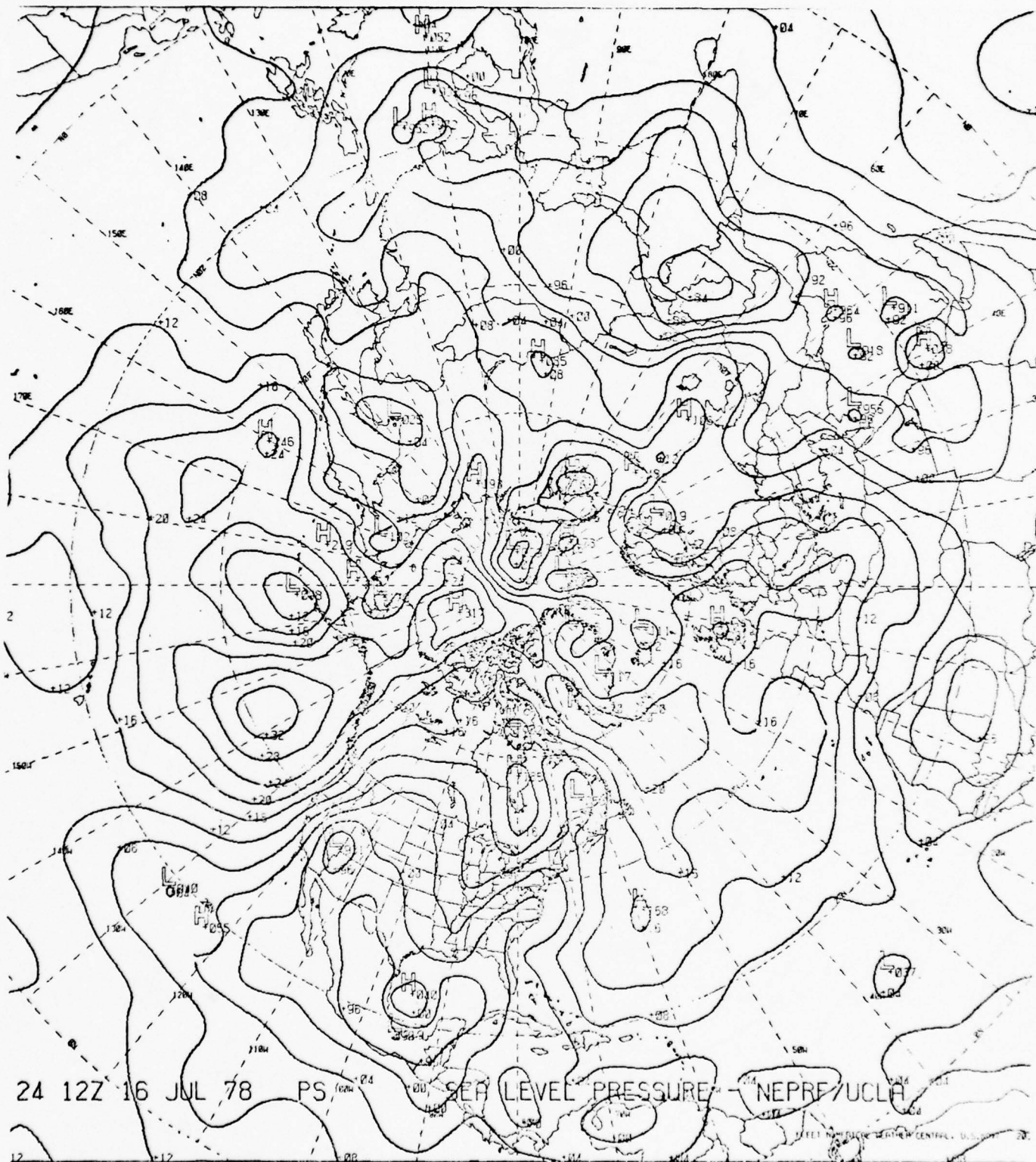
Figure 20.   24-hr. Forecast Sea Level Pressure for N. Hem.

With Assimilation

33

24 12Z 16 JUL 78   PS   SEA LEVEL PRESSURE - (NEPRF/UCLA
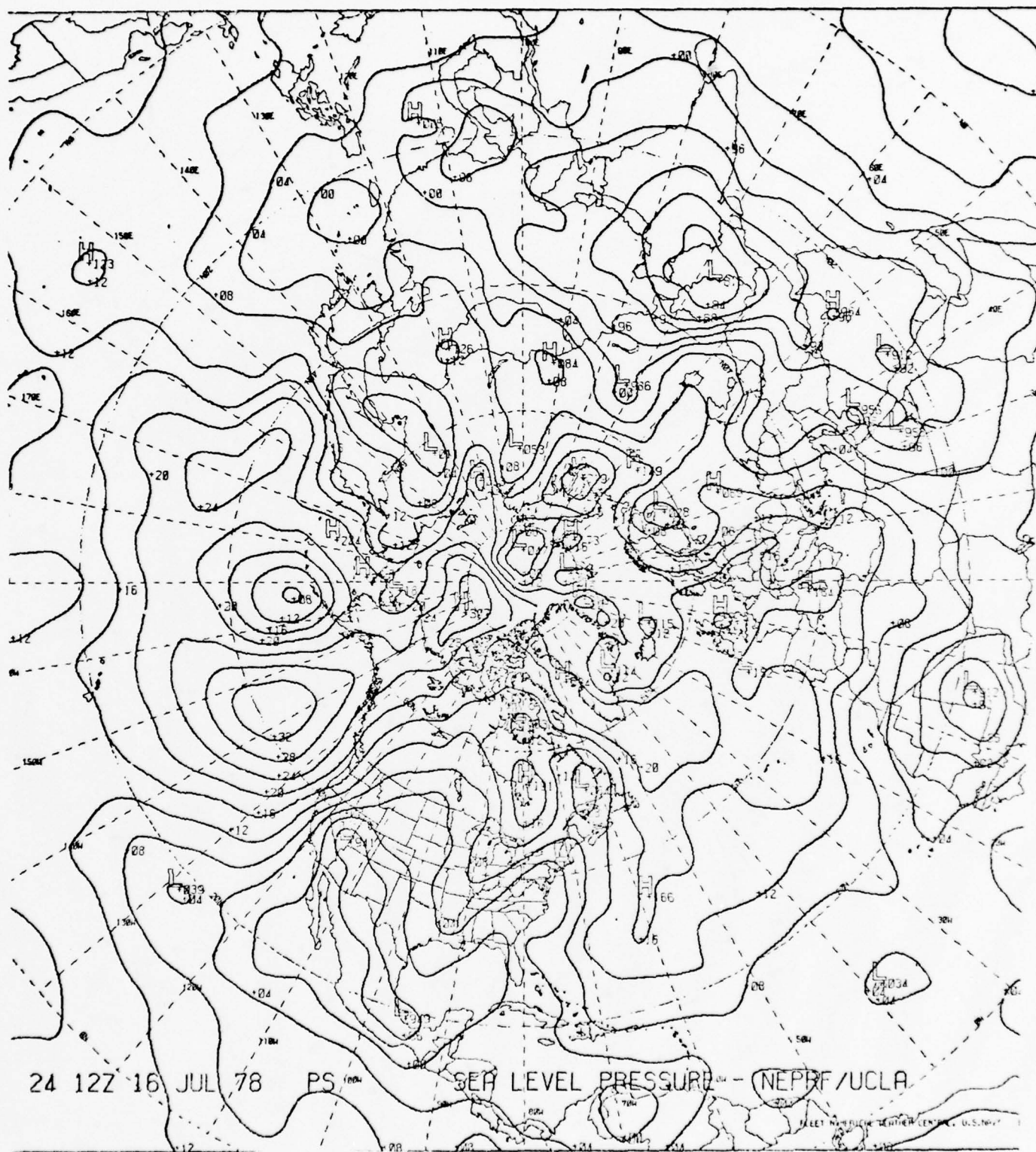
Figure 21.   24-hr. Forecast Sea Level Pressure for N. Hem.

Without Assimilation

34

24 12Z 16 JUL 78   S. H: SFC   SEA LEVEL PRESSURE - NEPRF/UCLA

FLEET NUMERICAL WEATHER CENTRAL, U.S. NAVY
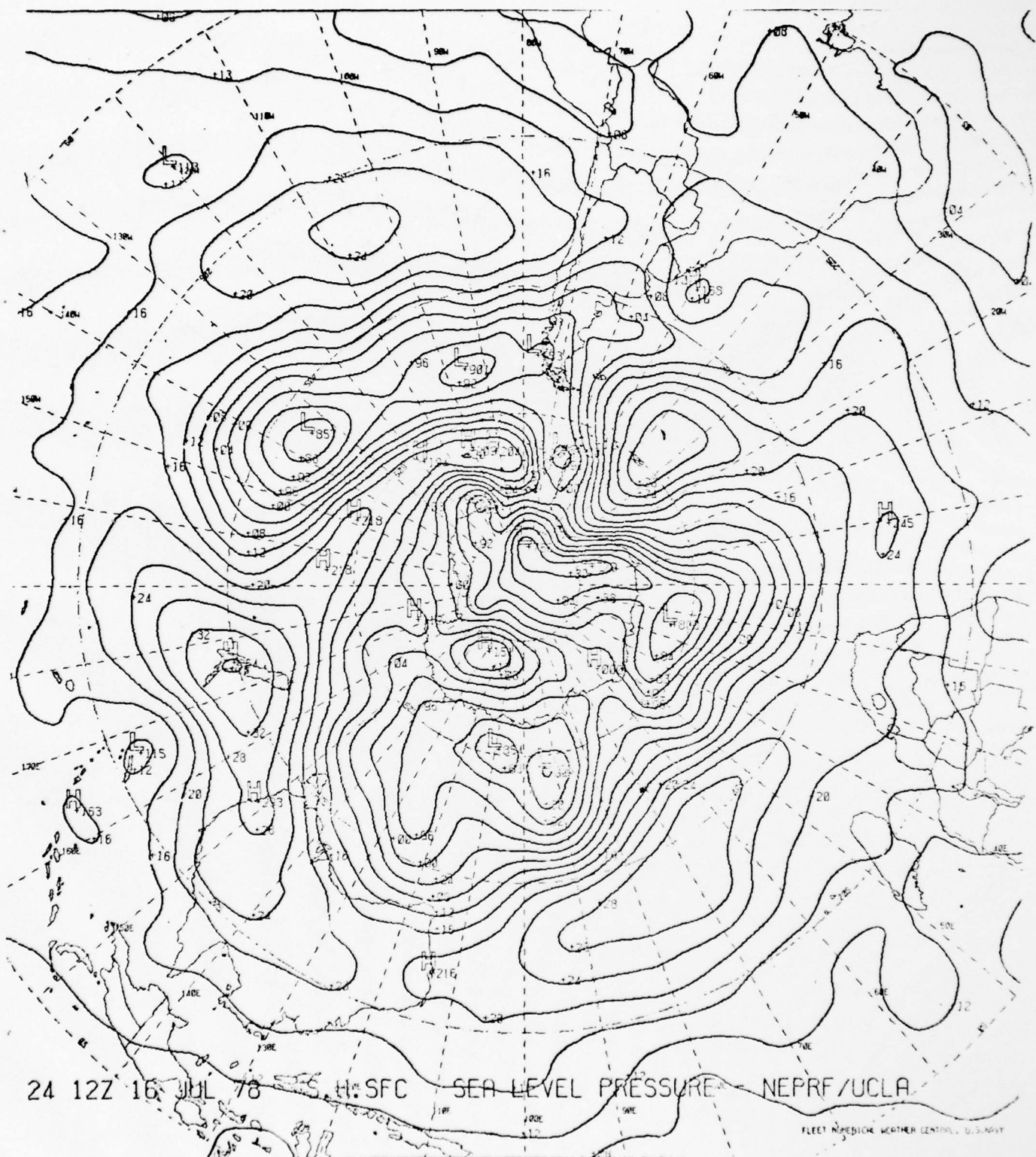
Figure 22.   24-hr. Forecast Sea Level Pressure for S. Hem.

With Assimilation

35

24 12Z 16 JUL 78   S. H. SFC   SEA LEVEL PRESSURE - NEPRF/UCLA
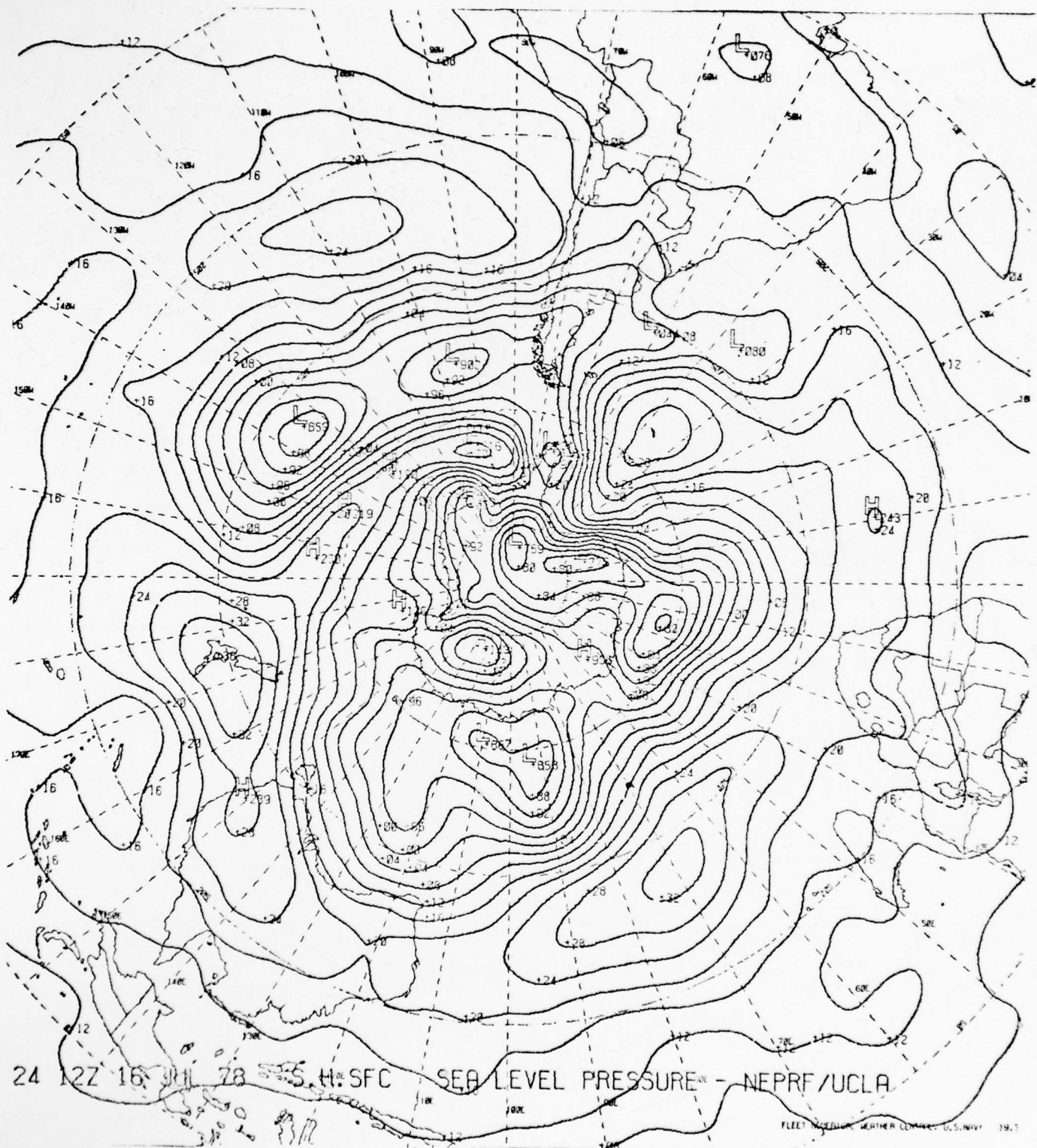
Figure 23.   24-hr. Forecast Sea Level Pressure for S. Hem.

Without Assimilation

48 12Z 16 JUL 78   D 500 M GEOPOTENTIAL AT 500 MBS - NEPRF/UCLA
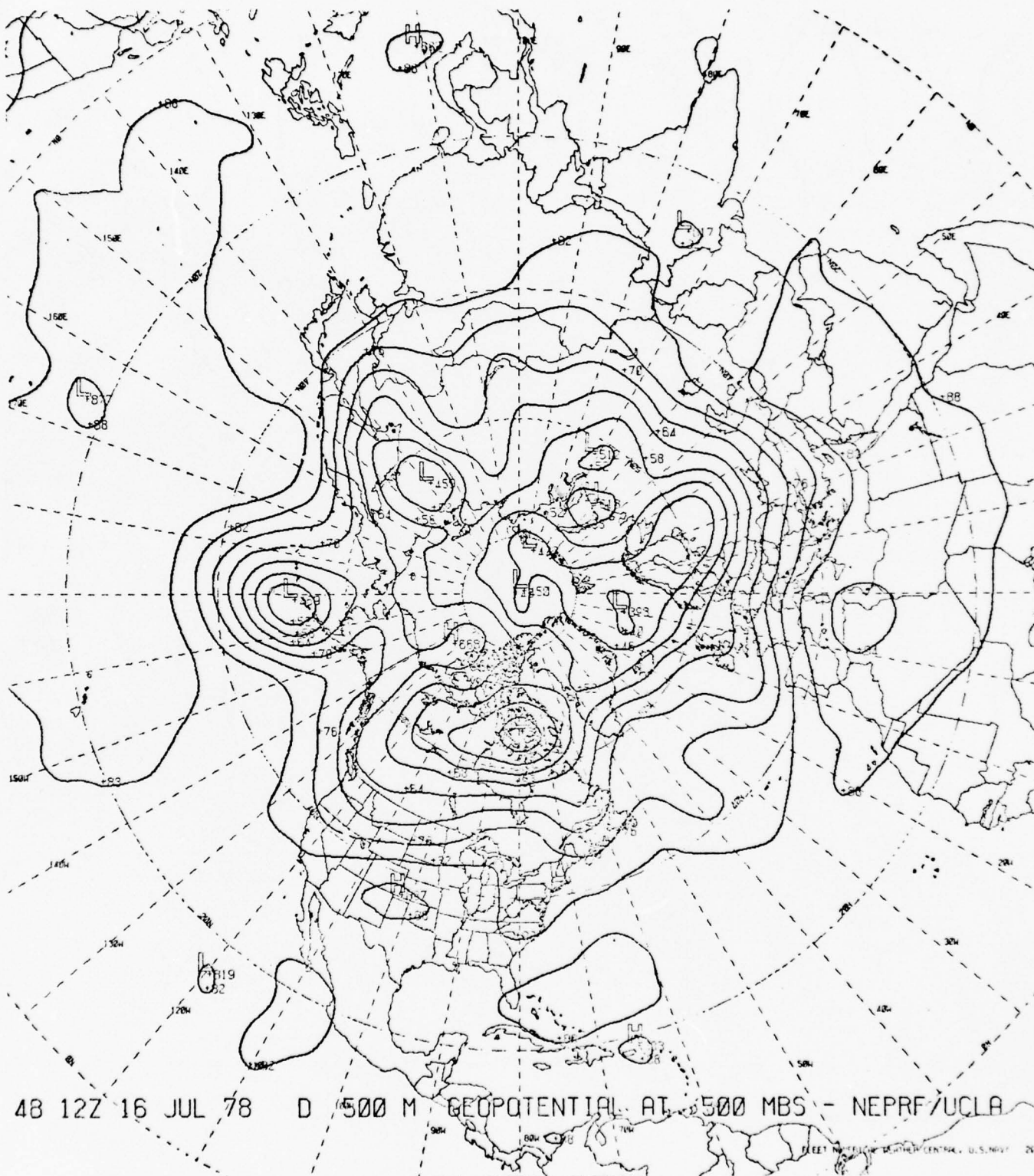
Figure 24.   48-hr. Forecast 500 mb Geopotential Height for N. Hem.

With Assimilation

37

48 12Z 16 JUL 78   D 500 M GEOPOTENTIAL AT 500 MBS - NEPRF/UCLA
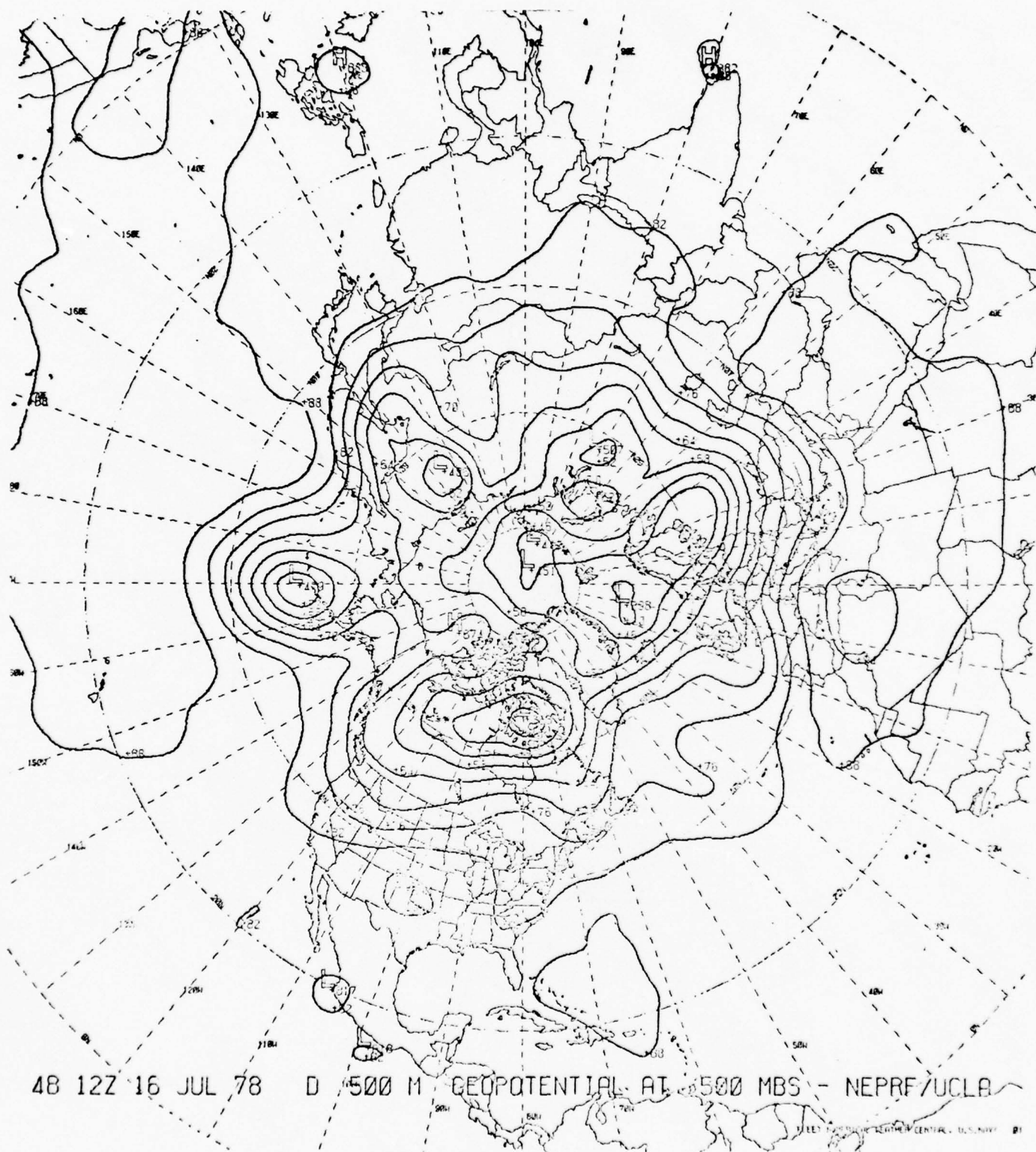
Figure 25. 48-hr. Forecast 500 mb Geopotential Height for N. Hem.

Without Assimilation

38

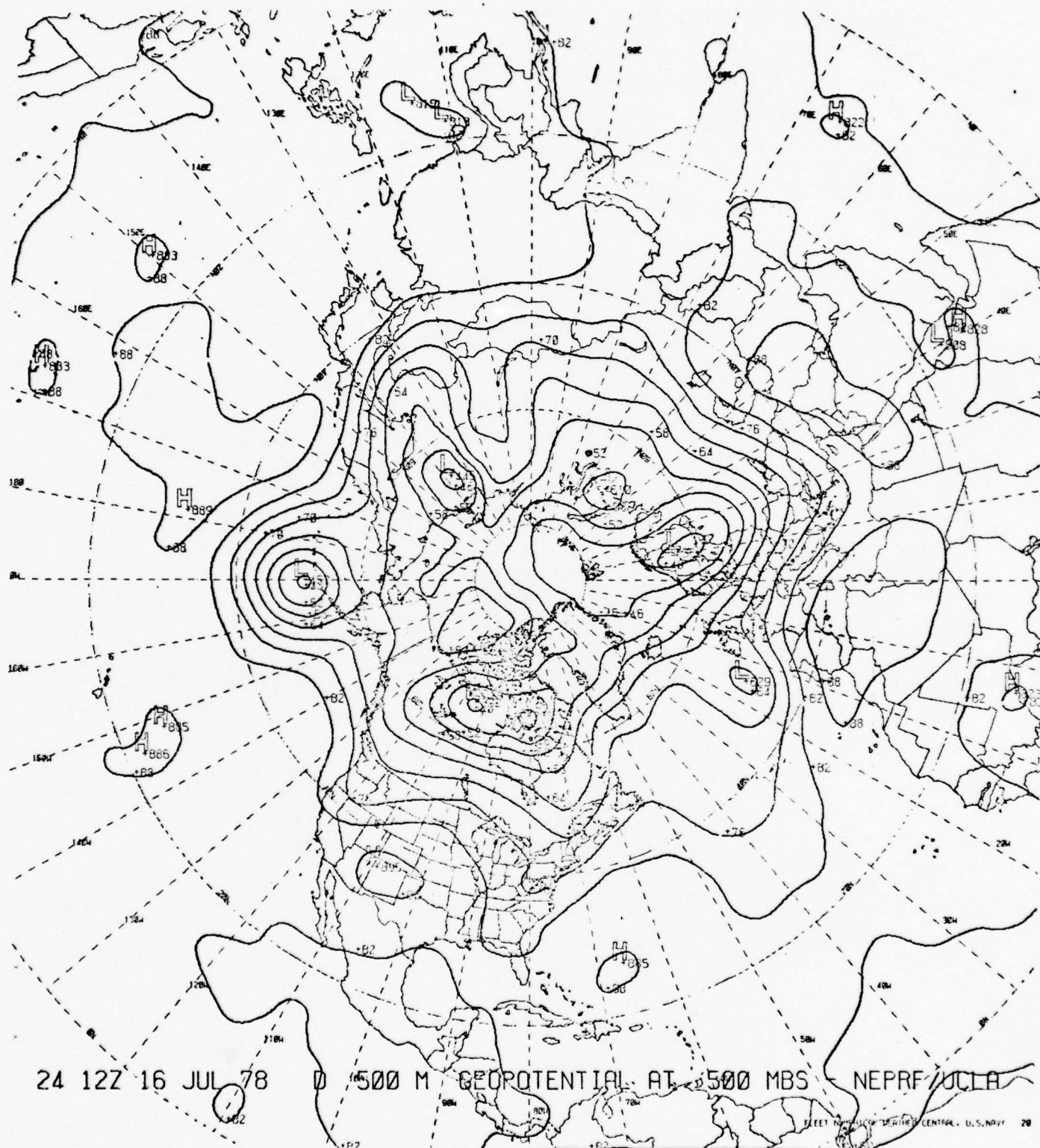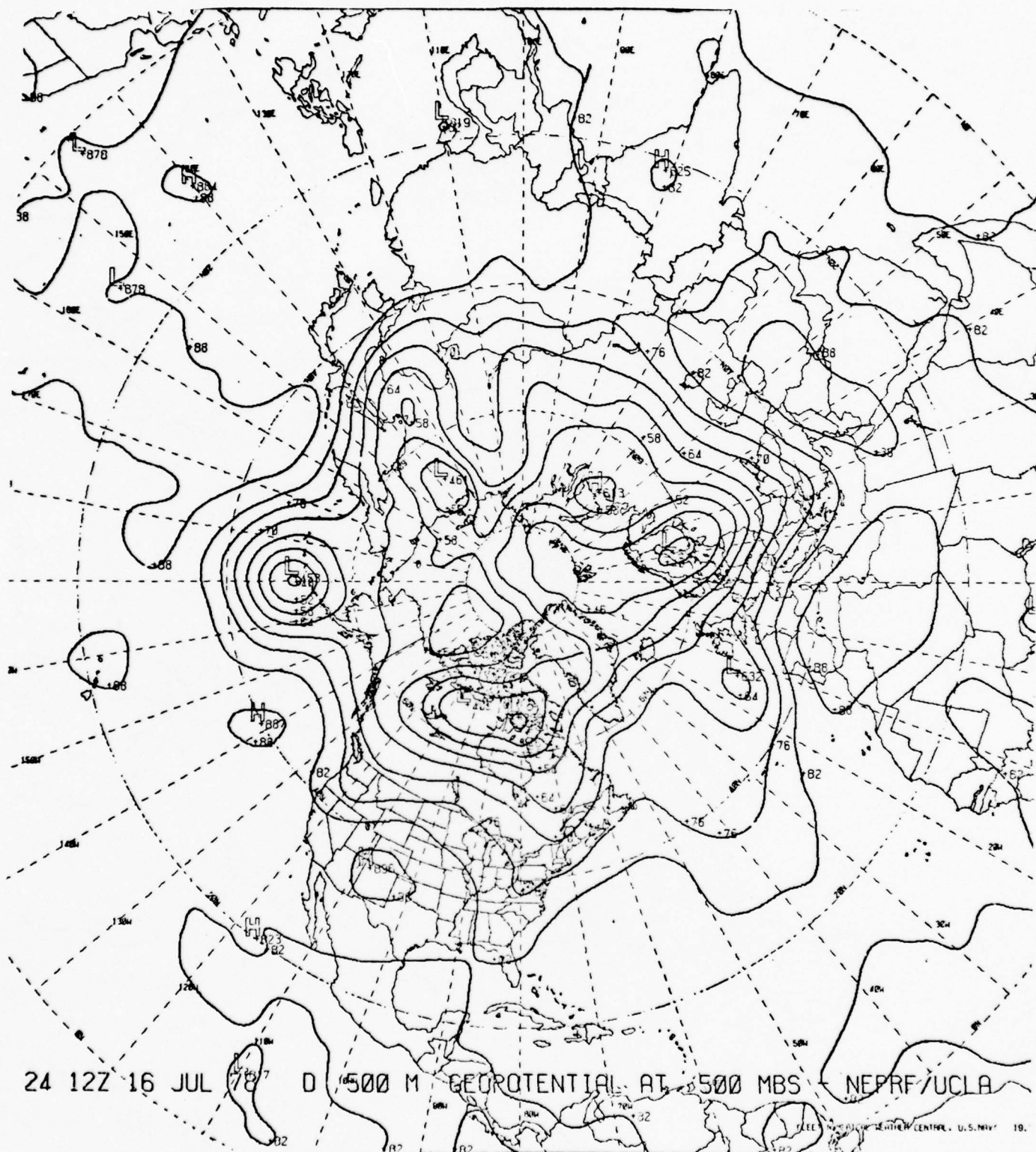48 12Z 16 JUL 78 D 500 M GEOPOTENTIAL AT 500 MBS - NEPRF/UCLA

Figure 26. 48-hr. Forecast 500 mb Geopotential Height for S. Hem.

With Assimilation

39

Figure 27. 48-hr. Forecast 500 mb Geopotential for S. Hem.

Without Assimilation

40

48 12Z 16 JUL 78   PS   SEA LEVEL PRESSURE - NEPRF/UCLA
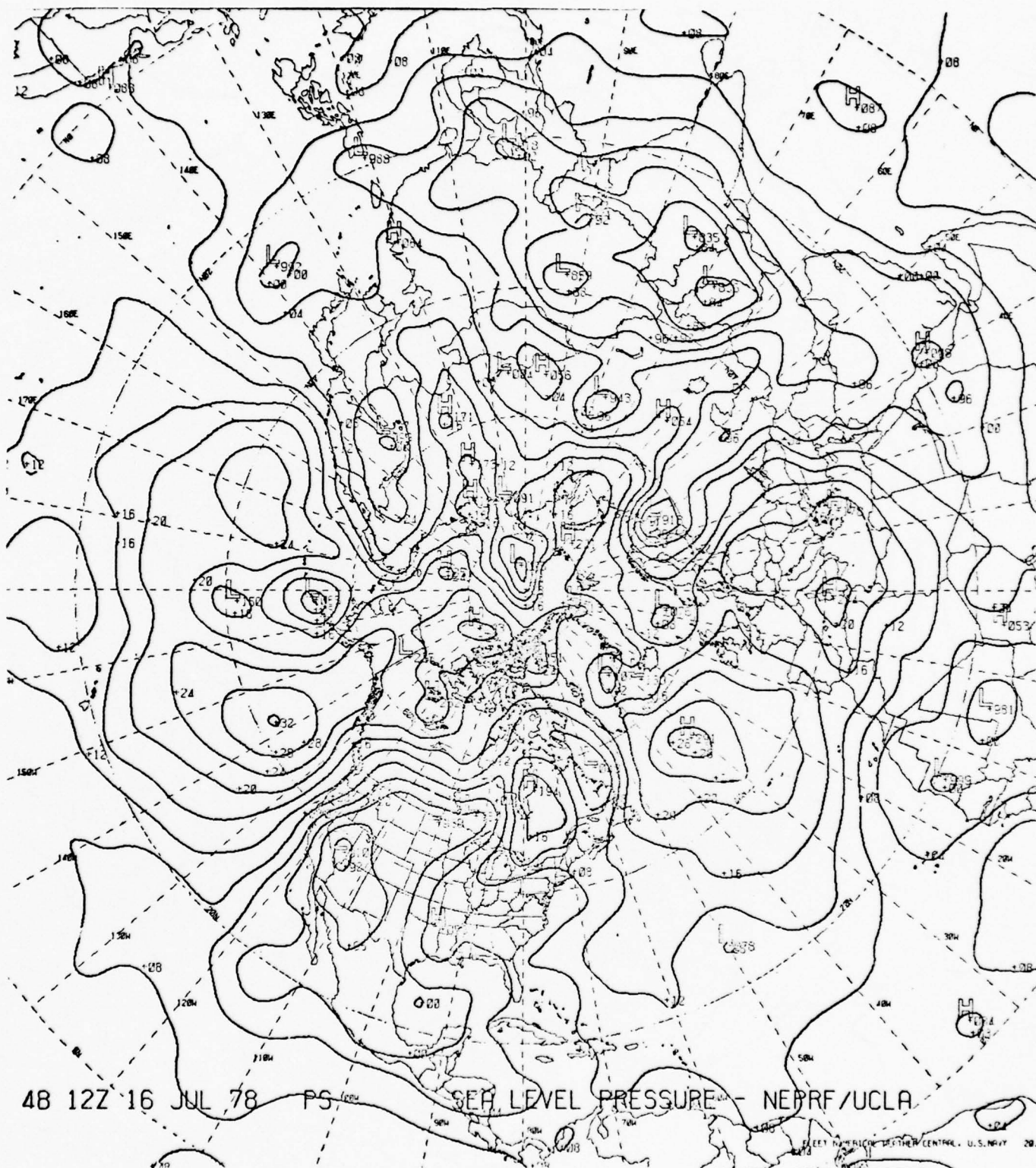
Figure 28.   48-hr. Forecast Sea Level Pressure for N. Hem.

With Assimilation

41

48 12Z 16 JUL 78   PS   SEA LEVEL PRESSURE - NEPRF/UCLA
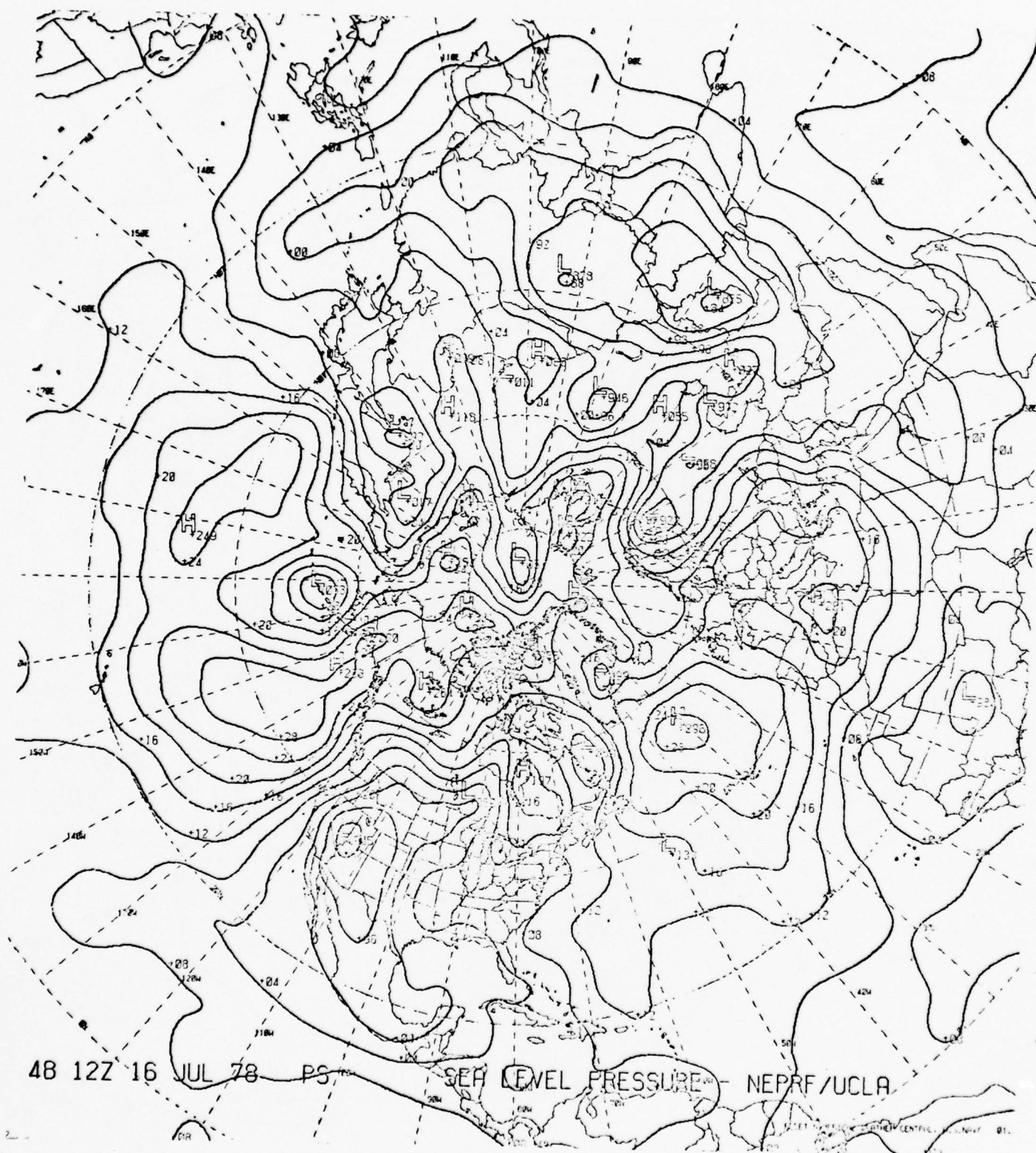
Figure 29.   48-hr. Forecast Sea Level Pressure for N. Hem.

Without Assimilation

42

48 12Z 16 JUL 78   S.H.SFC   SEA LEVEL PRESSURE - NEPRF/UCLA
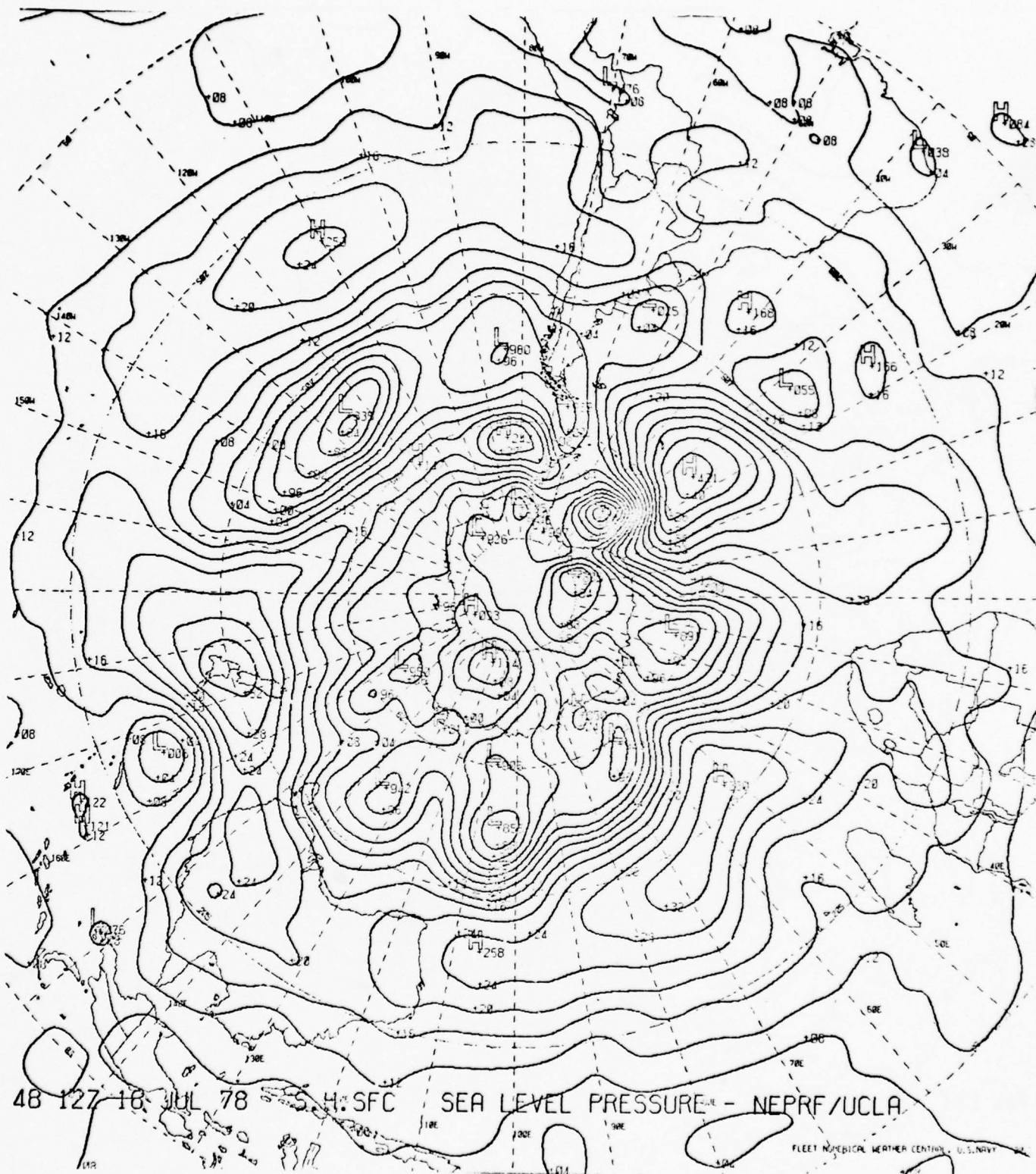
Figure 30.   48-hr. Forecast Sea Level Pressure for S. Hem.

With Assimilation

43

48 12Z 16 JUL 78   S. H. SFC   SEA LEVEL PRESSURE - NEPRF/UCLA
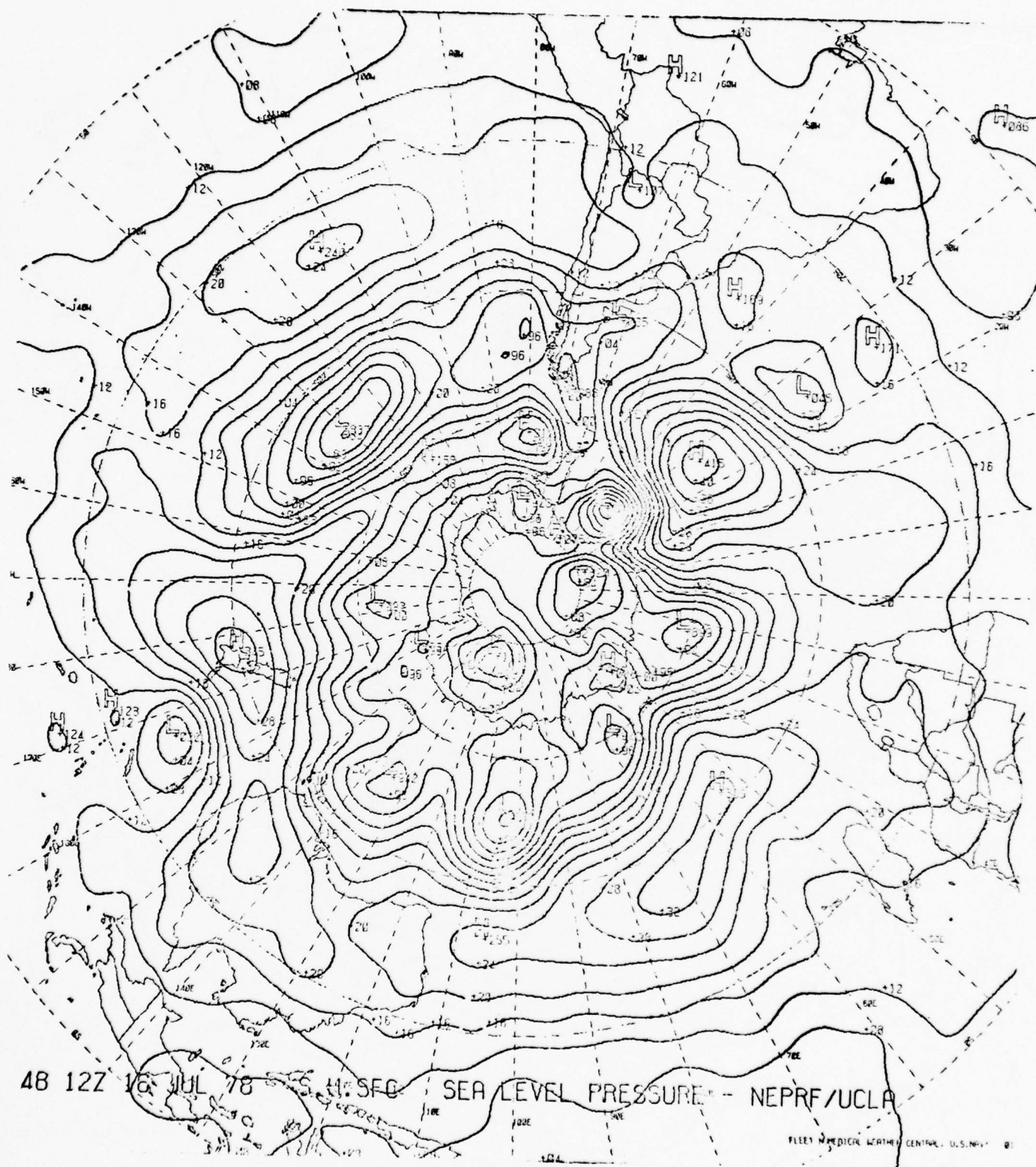
Figure 31.   48-hr. Forecast Sea Level Pressure for S. Hem.

With Assimilation

44

Notice in Figure 11 that after interpolation the
Argentine low is present at the 500 mb level and has prac-
tically the same depth as in the run with satellite data.
This fortuitous outcome must have resulted from the varia-
tional algorithm used in the interpolation. As a result,
there is very little difference between the two forecasts.
Other differences which appear in the results of the initial-
ization programs were also reduced by the interpolation.

This result seems to suggest that the temperature
analysis, especially at high levels, is controlling the mass
distribution which results from the variational interpolation.
Since the assimilation technique altered only the geopoten-
tials, its influence is being overruled by the temperatures
during the interpolation.

It can be seen from Figures 16 through 31 that the
two forecasts made with and without the satellite data
influence are very similar. This circumstance obviates any
discussion of the accuracy of the forecast, since it is
obvious that no significant improvement was wrought by the
satellite data assimilation.

5. RECOMMENDATIONS

The fact that a significant improvement in the fields resulting from the initialization model was demonstrated gives hope that a positive impact on the forecast might be obtained. Toward this end, we recommend that the vertical interpolation procedure in the forecast model be reviewed. Even though the effect of the interpolation in the run without satellite data was to improve the forecast, there is no assurance that improvement will always result.

Further testing should be done with this scheme to clarify its effectiveness.

6. BAROCLINIC PRIMITIVE EQUATION MODEL

A global baroclinic primitive equation model using spherical coordinates has been developed in order to perform the proposed research. This model employs simple finite differencing and uses variational algorithms in order to conserve total energy and mass. Furthermore, it has been programmed using disk input and output operations so that only a fraction of the model occupies the central memory of the computer at a given time. Thus, it is possible to run a global model even on a computer with limited amounts of central memory. In this section the model itself is described as well as its programming flow.

Model Description

Units: M G S.

Vertical Structure: KM specifies the number of levels where $\vec{v}$ and T are carried. $\sigma = 0$ at 250 mb (P_t) and $\sigma = 1$ at the surface (P_s). $\dot{\sigma} = 0$ at $\sigma = 0$ and $\sigma = 1$. The model consists of KM layers each $\frac{1}{KM}$ thick. The vertical structure is illustrated in Fig. 32a.

Horizontal Structure: JM specifies the number of grid-points around a latitude ring (e.g., JM=48 implies 7.5° grid spacing). IM is set to JM/2 + 2 giving a constant latitude-longitude

47
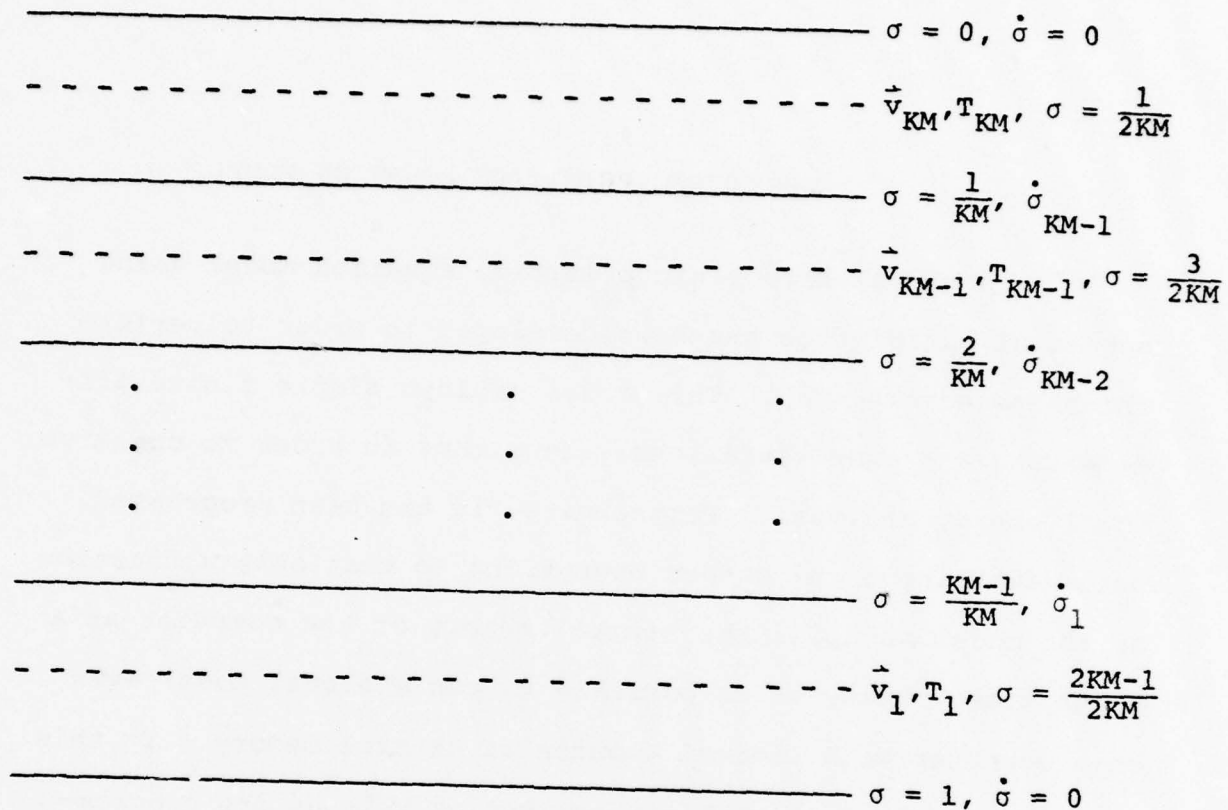
Fig. 32a. Vertical structure of the model.

The vertical levels are labeled:

$\sigma = 0, \; \dot{\sigma} = 0$

$\vec{v}_{KM}, T_{KM}, \; \sigma = \frac{1}{2KM}$

$\sigma = \frac{1}{KM}, \; \dot{\sigma}_{KM-1}$

$\vec{v}_{KM-1}, T_{KM-1}, \; \sigma = \frac{3}{2KM}$

$\sigma = \frac{2}{KM}, \; \dot{\sigma}_{KM-2}$

$\sigma = \frac{KM-1}{KM}, \; \dot{\sigma}_1$

$\vec{v}_1, T_1, \; \sigma = \frac{2KM-1}{2KM}$

$\sigma = 1, \; \dot{\sigma} = 0$

Fig. 32b. Horizontal structure of the model.

$u_{1,48}$ $T_{1,48}$	$u_{1,1}$ $T_{1,1}$	$u_{1,2}$ $T_{1,2}$	86.25° N
$v_{1,48}$	$v_{1,1}$	$v_{1,2}$	90° N
$u_{2,48}$ $T_{2,48}$	$u_{2,1}$ $T_{2,1}$	$u_{2,2}$ $T_{2,2}$	86.25° N
$v_{2,48}$	$v_{2,1}$	$v_{2,2}$	82.5° N
$u_{3,48}$ $T_{3,48}$	$u_{3,1}$ $T_{3,1}$	$u_{3,2}$ $T_{3,2}$	78.75° N

48

grid with two fictitious latitude rings near the poles. The fictitious rings are carried in the model in order to simplify the coding. The Arakawa (C) lattice is used as illustrated for IM=26 and JM=48 in Fig. 32b.

Values of ϕ, π and $\dot{\sigma}$ are carried at the grid points labeled T. The values of v at the north and south poles are seldom needed since $\cos \theta = 0$ for $\theta = \pm 90°$. This will be seen more clearly when the primitive equations are written out in flux form for $(\lambda, \theta, \sigma)$ coordinates. There are IM latitude rings where T, ϕ, π, and $\dot{\sigma}$ are carried. For JM=48, $T_{1,j} = T_{2,j\pm24}$ and $T_{26,j} = T_{25,j\pm24}$. The values of ϕ, π, and $\dot{\sigma}$ are computed in a similar fashion for the fictitious latitude rings. The values of v at the north and south poles, respectively, are

$$v_{1,j} = \frac{v_{2,j} - v_{2,j\pm24}}{2} \text{ and } v_{25,j} = \frac{v_{24,j} - v_{24,j\pm24}}{2}$$

Primitive Equations: The primitive equations are written in flux form using $(\lambda, \theta, \sigma)$ co-ordinates. Before describing the equations some preliminary definitions must be made:

$p = \pi\sigma + p_t$ where $\pi = p_s - p_t$,

$T = \theta \left(\frac{p}{1000}\right)^\kappa$, and

$\frac{\partial \phi}{\partial \sigma} = -\pi\alpha$

The primitive equations are:

Mass Continuity

$$\frac{\partial \pi}{\partial t} + \frac{1}{a \cos \theta} \left[\frac{\partial}{\partial \lambda} (\pi u) + \frac{\partial}{\partial \theta} (\pi v \cos \theta)\right] + \frac{\partial}{\partial \sigma} (\pi\dot{\sigma}) = 0 \qquad (17)$$

49

Equations of Motion

$$\frac{\partial}{\partial t}(\pi u) + \frac{1}{a \cos \theta}\left[\frac{\partial}{\partial \lambda}(\pi u^2) + \frac{\partial}{\partial \theta}(\pi \, u \, v \cos \theta)\right] + \frac{\partial}{\partial \sigma}(\pi u \dot{\sigma})$$

$$+ \frac{\pi}{a \cos \theta}\left[\frac{\partial \phi}{\partial \lambda} + \sigma \alpha \frac{\partial \pi}{\partial \lambda}\right] - \left[f + \frac{u \tan \theta}{a}\right]\pi \, v = \pi \, F_\lambda \qquad (18)$$

$$\frac{\partial}{\partial t}(\pi v) + \frac{1}{a \cos \theta}\left[\frac{\partial}{\partial \lambda}(\pi \, u \, v) + \frac{\partial}{\partial \theta}(\pi \, v^2 \cos \theta)\right] + \frac{\partial}{\partial \sigma}(\pi \, v \, \dot{\sigma})$$

$$+ \frac{\pi}{a}\left[\frac{\partial \phi}{\partial \theta} + \sigma \, \alpha \, \frac{\partial \pi}{\partial \theta}\right] + \left[f + \frac{u \tan \theta}{a}\right]\pi \, u = \pi \, F_\theta \qquad (19)$$

Thermodynamic Equation

$$\frac{\partial}{\partial t}(\pi T) + \frac{1}{a \cos \theta}\left[\frac{\partial}{\partial \lambda}(\pi u T) + \frac{\partial}{\partial \theta}(\pi v T \cos \theta)\right] + \left(\frac{p}{1000}\right)^K \frac{\partial}{\partial \sigma}(\pi \dot{\sigma} \, \theta)$$

$$+ \frac{\pi^2 \sigma \alpha}{c_p}\left[\frac{1}{a \cos \theta}\left\{\frac{\partial u}{\partial \lambda} + \frac{\partial}{\partial \theta}(v \cos \theta)\right\} + \frac{\partial \dot{\sigma}}{\partial \sigma}\right] = \frac{\pi Q}{c_p}. \qquad (20)$$

In the model centered-time and centered-space differencing is used along with these equations in order to forecast π, u, v, and T.

The forecast for π at time n+1 must be made first so that a diagnostic equation for $\dot{\sigma}$ at time n can be solved and the result used in forecasting u, v, and T at time n+1. The values of ϕ at each time step are found using the hydrostatic equation ($\frac{\partial \phi}{\partial \sigma} = -\pi \alpha$).

Variational Conservation of Mass and Energy: Using the calculus of variations the π, u, v, and T fields are adjusted at each time step so that the initial mass and energy input to the model are conserved. For energy the functional to be minimized is:

50

$$J = \Sigma\Sigma\Sigma \ \tilde{\alpha}\Delta A \ (u-\tilde{u})^2 + \Sigma\Sigma\Sigma \ \tilde{\alpha}\Delta A \ (v-\tilde{v})^2 + \Sigma\Sigma\Sigma \ \tilde{\beta}\Delta A \ (T-\tilde{T})^2$$

$$+ \ \lambda_E \ \{\Sigma\Sigma\Sigma [c_p \pi T \Delta A + \bar{\pi}^j \Delta A \frac{u^2}{2} + \bar{\pi}^i \Delta A \frac{v^2}{2}] - TE_o\},$$

where $TE_o = \Sigma\Sigma\Sigma c_p \pi_o T_o \Delta A + \Sigma\Sigma\Sigma \bar{\pi}_o^{\ j} \Delta A \frac{u_o^2}{2} + \Sigma\Sigma\Sigma \bar{\pi}_o^{\ i} \Delta A \frac{v_o^2}{2}$

(π_o, T_o, u_o, and v_o are all initial values and ΔA is the area increment associated with the appropriate grid point).

The ratio of $\tilde{\alpha}/\tilde{\beta}$ is taken to be $\tilde{T}/c_p \thicksim 1/3.68$. The resulting corrections for u, v, and T applied at each time step are:

$$u = \tilde{u} \ (1 - \frac{\lambda_E \bar{\pi}^j}{2\tilde{\alpha}})$$

$$v = \tilde{v} \ (1 - \frac{\lambda_E \bar{\pi}^i}{2\tilde{\alpha}})$$

$$T = \tilde{T} - \frac{\lambda_E \ \check{c}_p \pi}{2\tilde{\beta}}$$

An approximate solution for λ_E is used:

$$\lambda_E = \frac{\Sigma\Sigma\Sigma (c_p \pi \Delta A \tilde{T} + \bar{\pi}^j \Delta A \ \frac{\tilde{u}^2}{2} + \bar{\pi}^i \Delta A \ \frac{\tilde{v}^2}{2}) - TE_o}{\Sigma\Sigma\Sigma (\frac{c_p^2 \pi^2 \Delta A}{2\tilde{\beta}} + \frac{\bar{\pi}^{j2} \Delta A \tilde{u}^2}{2\tilde{\alpha}} + \frac{\bar{\pi}^{i2} \Delta A \tilde{v}^2}{2\tilde{\alpha}})}$$

For mass the functional to be minimized is:

$$I = \underset{ij}{\Sigma\Sigma} \ \Delta A (\pi - \tilde{\pi})^2 + \lambda_M [\underset{ij}{\Sigma\Sigma} \ \pi \Delta A - \underset{ij}{\Sigma\Sigma} \pi_o \Delta A]$$

where π_o is the initial value for π. The resulting correction to the π-field is:

$$\pi = \tilde{\pi} - \frac{\lambda_M}{2} \quad \text{where}$$

$$\lambda_M = \frac{2[\Sigma\Sigma\tilde{\pi}\Delta A - \Sigma\Sigma\pi_o\Delta A]}{\Sigma\Sigma\Delta A}$$

This correction is also applied each time step. In order to apply the two corrections simultaneously, λ_E is slightly adjusted by the ratio $(\Sigma\Sigma\bar{\pi}\Delta A/\Sigma\Sigma\pi_o\Delta A)$ in order to compensate for the adjustment to π and its effect upon the energy calculations.

Filtering: Two distinct and very different types of filtering are used in the model. Robert time filtering is employed to eliminate the "two-solution" problem that leapfrog time-differencing would induce. The prognostic quantities u, v, T, and π are filtered each time step using:

$$\bar{F}_n = (1 - \alpha)\, F_n + \frac{\alpha}{2}\, [\bar{F}_{n-1} + F_{n+1}] \text{ and } \alpha = 0.2.$$

In order to ensure the computational stability, space filtering must be performed in the vicinity of the poles due to the reduction in size of the horizontal grid spacing caused by the equal latitude-longitude grid. In this model Fourier filtering is employed for each of the prognostic variables at every time step for latitudes poleward from and including 45°. Table 1 indicates the maximum wave number passed for a given variable and latitude when IM = 26, JM = 48, and Δt = 450 sec.

Although many papers on the subject of spherical grids and space filtering would indicate that a larger time-step may be used and computational stability maintained, it was found that this was not the case for a homogeneous atmosphere and Phillips' initial conditions for a 4-wave global pattern. It

52

Table 1. Maximum wave number passed during Fourier filtering.

Variable	Latitude					
	86.25	78.75	71.25	63.75	56.25	48.75
u, π, T	2	6	10	14	18	21
v	4	8	12	16	19	23
	82.50	75.00	67.50	60.00	52.50	45
	Latitude					

is suspected that under less extreme conditions than those used to test this model a larger time-step may be employed.

MODEL PROGRAMMING FLOW

In order to make efficient use of computer time and space, this model utilizes circular buffers. Essentially, only six data blocks are carried in core at one time with constant input from and output to disk being performed simultaneously and wherever possible covered by computation. Each data block can be thought of as a one-dimensional array dimensioned by NVAR = (8*KM + 3)* JM and contains all of the necessary variables for one "latitude ring" (actually, due to the staggered grid v is at a different latitude). The location within this array of a particular variable is determined by the offsets described in Table 2.

The arrays AO and AN are dimensioned by 4*NVAR and 2*NVAR, respectively. At a given time array AO contains the
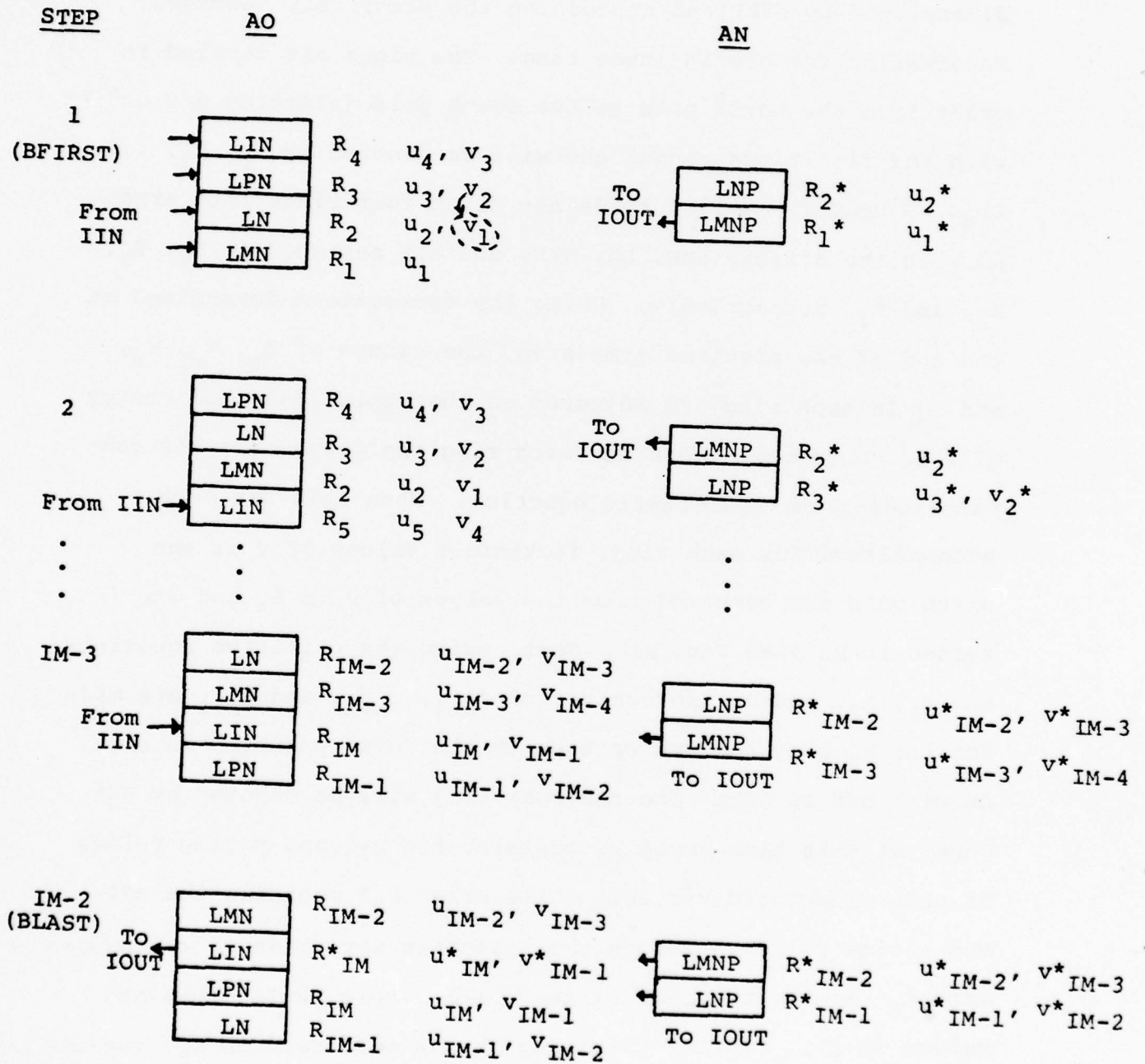
53

Table 2. Offsets of Variables in Arrays AO and AN

Constant Field	Levels	Name of Offset	Value of Offset
Geopotential of terrain ht.	1	MGZ	0
One Time-level Fields			
Geopotential heights, ϕ	KM	MPHI	$\dot{}$ JM
Vertical Velocities, $\dot{\sigma}$	KM	MWV	$(KM + 1)*JM$
Two Time-level Fields			
Terrain Pressure, π_{n-1}	1	MPTNM	$(2*KM + 1)*JM$
Terrain Pressure, π_n	1	MPTN	$(2*KM + 2)*JM$
u-wind, u_{n-1}	KM	MUNM	$(2*KM + 3)*JM$
u-wind, u_n	KM	MUN	$(3*KM + 3)*JM$
v-wind, v_{n-1}	KM	MVNM	$(4*KM + 3)*JM$
v-wind, v_n	KM	MVN	$(5*KM + 3)*JM$
Temperature, T_{n-1}	KM	MTNM	$(6*KM + 3)*JM$
Temperature, T_n	KM	MTN	$(7*KM + 3)*JM$

three latitude rings needed to make a forecast for the middle
ring while the next latitude ring that will be used is being
read from disk into its remaining space. At a given time the
forecast for the middle latitude ring is being computed and
placed in array AN while the forecast latitude ring for the
previous time-step is being written to disk. The location with-
in arrays AO and AN of the various latitude rings is also deter-
mined by the offsets LMN, LN, LPN, and LIN (for AO) and LMNP
and LNP (for AN). In the following combination of text and
illustrations, the programming flow of this model will be des-
cribed.

At the beginning of a particular time-step the disk file IIN contains IM records, each record consisting of an array dimensioned by NVAR and containing the previously described information for one latitude ring. The rings are carried in order from the north pole to the south pole (starting and ending with the fictitious rings) and will be denoted by R_1, R_2, ..., R_{IM}. Subroutine BFIRST reads the first four rings into array AO with the offsets LMN, LN, LPN, and LIN assigned to R_1, R_2, R_3, and R_4, respectively. Using the corrections determined at the end of the previous time-step, the values of π_n, u_n, v_n, and T_n in each ring are adjusted so that total mass and energy will be conserved. Then for each ring the value of ϕ_n is computed using the hydrostatic equation. When this has been accomplished for each ring, fictitious values of v at the north pole are computed from the values of v in R_3 and are inserted in R_2 (see Fig. 33). Next, using the primitive equations and R_1, R_2, and R_3, forecasts for π_{n+1}, u_{n+1}, and T_{n+1} are made for the R_2 ring and are written in the "n-1" position in array AN with offset LNP. The forecast ring will be denoted by $R_2{}^*$. Thus, at this time array R_2 contains the n-1 and n time values of each prognostic variable while array $R_2{}^*$ contains the n+1 and n time values. Before the forecasts were made R_2 was copied into $R_2{}^*$ so the forecast values (n+1) simply replace the old values (n-1). Fourier filtering is now performed in $R_2{}^*$ for the new forecast values (n+1) of π, u, and T. Then, using the n+1 and n values in $R_2{}^*$ and the n-1 value in R_2, the n value of $R_2{}^*$

55

Fig. 33. P.E. Model Programming Flow

Note: (u_i denotes presence of π_i, T_i, ϕ_i, & $\dot{\sigma}_i$)

| STEP | AO | | | | AN | | | |

1
(BFIRST)

From IIN →

LIN	R_4	u_4, v_3
LPN	R_3	u_3, v_2
LN	R_2	u_2, v_1
LMN	R_1	u_1

To IOUT ←

| LNP | $R_2{}^*$ | $u_2{}^*$ |
| LMNP | $R_1{}^*$ | $u_1{}^*$ |

2

From IIN →

LPN	R_4	u_4, v_3
LN	R_3	u_3, v_2
LMN	R_2	u_2 v_1
LIN	R_5	u_5 v_4

To IOUT ←

| LMNP | $R_2{}^*$ | $u_2{}^*$ |
| LNP | $R_3{}^*$ | $u_3{}^*$, $v_2{}^*$ |

.
.
.

.
.
.

IM-3

From IIN →

LN	R_{IM-2}	u_{IM-2}, v_{IM-3}
LMN	R_{IM-3}	u_{IM-3}, v_{IM-4}
LIN	R_{IM}	u_{IM}, v_{IM-1}
LPN	R_{IM-1}	u_{IM-1}, v_{IM-2}

| LNP | R^*_{IM-2} | u^*_{IM-2}, v^*_{IM-3} |
| LMNP | R^*_{IM-3} | u^*_{IM-3}, v^*_{IM-4} |

← To IOUT

IM-2
(BLAST)

To IOUT ←

LMN	R_{IM-2}	u_{IM-2}, v_{IM-3}
LIN	R^*_{IM}	u^*_{IM}, v^*_{IM-1}
LPN	R_{IM}	u_{IM}, v_{IM-1}
LN	R_{IM-1}	u_{IM-1}, v_{IM-2}

| LMNP | R^*_{IM-2} | u^*_{IM-2}, v^*_{IM-3} |
| LNP | R^*_{IM-1} | u^*_{IM-1}, v^*_{IM-2} |

To IOUT

is replaced by a Robert time-filtered value. Computations necessary for the determination of the mass and energy constraint adjustments are now made using the n+1 values in R_2^* and finally the values of R_2^* are used to generate the fictitious ring R_1^* and the ring R_1^* is written to disk file IOUT.

Steps 2 to IM-3 are all similar in nature. Each step begins with the next latitude ring needed being read from disk IIN into array AO, offset LIN and the previous forecast being written to disk IOUT from array AN, offset LMNP (see Fig. 33). These input and output operations will be covered by computations. Note that for step 2 (and similarly for all succeeding steps) the rings R_2, R_3, and R_4 and the ring R_2^* remain in the same place in arrays AO and AN that they occupied during the previous step while the values of the offsets are rotated to indicate their "new positions". The ring in array AO, offset LN is copied to array AN, offset LNP and forecasts for π_{n+1}, u_{n+1}, v_{n+1}, and T_{n+1} are made. The appropriate Fourier filtering (if any) is then applied to the forecast values (n+1) in the R* ring and the present values (n) in the R* ring are time-filtered using the n-1, n, and n+1 values contained in the R and R* rings. Using the n+1 values in the R* ring, the necessary computations for the mass and energy adjustments to be made on the next time-step are performed. Finally, the mass and energy adjustments determined from the previous time step are applied to the values of π_n, u_n, v_n, and T_n in the R ring which has been

read into array AO, offset LIN, and the ϕ_n values for this ring are computed using the hydrostatic equation.

Subroutine BLAST must be called in order to complete the forecast sequence for a time-step. First, R^*_{IM-2} is written to disk IOUT and, using the procedure described previously, rings R_{IM-2}, R_{IM-1}, and R_{IM} are used to produce ring R^*_{IM-1} (array AN, offset LNP). After this ring has been Fourier-filtered, time-filtered, and used to compute mass and energy adjustments, it too is written to disk IOUT. Finally, the values of ring R^*_{IM} are determined from ring R^*_{IM-1} and put in array AO, offset LIN. From there they are written to disk IOUT and the sequence is complete.

Upon completion of the forecast sequence for a time-step, the disk files IIN and IOUT are both rewound and their names switched. Thus, the disk upon which the forecasts were written becomes the new input disk while the old input disk will be used to house the next set of forecasts. After each time step the offsets for the two time-level fields are also switched (i.e.; MPTNM and MPTN, etc.) since during the forecast process the n+1 values replace the n-1 values while the n values remain in position. It should be noted in Fig. 33 that the variables u, π, and T are carried on IM latitude rings (2 fictitious), and v is carried on IM-1 rings (including the north and south poles). Also, the values of v carried on a given R or R^* ring are those north of the values for u, π, and T carried on the same ring.

58

7.   NOISE FREEZING FOR THE BAROCLINIC PRIMITIVE EQUATION MODEL

In section 2.3 it was shown that the phase speed of external gravity waves in a barotropic model could be reduced without significantly altering the speed of meteorological waves when the value of γ in (9) was adjusted from 1.0 to a value between 1.0 and 0.1. The speed of the gravity waves is proportional to the square root of the mean atmospheric depth, H. By reducing the modelled mean depth, the gravity waves are slowed without substantially affecting the waves of meteorological significance. Upon examination of (7)-(9) we can state that noise freezing is performed simply by decreasing the contribution of horizontal divergence to the tendency of the depth of the model atmosphere, h.

The implementation of noise freezing in a baroclinic model requires that the contribution of horizontal divergence to the surface pressure tendency be reduced without disrupting the horizontal gradients of π. This is done most easily by subtracting a constant from all values of π carried within the model. The constant is chosen to be as large as possible without causing negative or zero values of π. Since the equations of motion (18) and (19) and the thermodynamic equation (20) (repeated below) used in the model are written in flux form by adding the continuity equation, care must be taken so that the reduction of π does not improperly affect the values of other variables in the equations. In (18)-(20)

59

the variables indicated by arrows must not be affected by the reduction in π.

$$\frac{\partial(\pi u)}{\partial t} + \frac{1}{a\cos\theta}\left[\frac{\partial}{\partial\lambda}(\pi u^2) + \frac{\partial}{\partial\theta}(\pi uv\cos\theta)\right] + \frac{\partial}{\partial\sigma}(\pi u\dot{\sigma})$$
$$+ \frac{\pi}{a\cos\theta}\left[\frac{\partial\overset{\downarrow}{\phi}}{\partial\lambda} + \sigma\overset{\downarrow}{\alpha}\frac{\partial\pi}{\partial\lambda}\right] - \left[f + \frac{u\tan\theta}{a}\right]\pi v = \pi F_\lambda \tag{18}$$

$$\frac{\partial(\pi v)}{\partial t} + \frac{1}{a\cos\theta}\left[\frac{\partial}{\partial\lambda}(\pi uv) + \frac{\partial}{\partial\theta}(\pi v^2\cos\theta)\right] + \frac{\partial}{\partial\sigma}(\pi v\dot{\sigma})$$
$$+ \frac{\pi}{a}\left[\frac{\partial\overset{\downarrow}{\phi}}{\partial\theta} + \sigma\overset{\downarrow}{\alpha}\frac{\partial\pi}{\partial\theta}\right] + \left[f + \frac{u\tan\theta}{a}\right]\pi u = \pi F_\theta \tag{19}$$

$$\frac{\partial(\pi T)}{\partial t} + \frac{1}{a\cos\theta}\left[\frac{\partial}{\partial\lambda}(\pi uT) + \frac{\partial}{\partial\theta}(\pi vT\cos\theta)\right] + \left(\frac{\overset{\downarrow}{P}}{1000}\right)^\kappa \frac{\partial}{\partial\sigma}(\pi\sigma\overset{\downarrow}{\theta})$$
$$+ \frac{\pi^2\sigma\overset{\downarrow}{\alpha}}{c_p}\left[\frac{1}{a\cos\theta}\left\{\frac{\partial u}{\partial\lambda} + \frac{\partial}{\partial\theta}(v\cos\theta)\right\} + \frac{\partial\dot{\sigma}}{\partial\sigma}\right] = \frac{\pi Q}{c_p} \tag{20}$$

When these exceptions have been accounted for, the model can be run with noise freezing by simply subtracting a constant from the initial values of π.

A set of initial value conditions was prepared using NMC analyzed fields for 12Z 15 February 1976. These data were available at all of the standard levels at 2 1/2° intervals and were interpolated to the grid-points required by our model. Initial sea-level pressures were estimated from the heights of the 1000 mb surface. The u- and v- components of the wind were adjusted so that the initial mass divergence at each grid-point was zero and internal balancing was applied to adjust the geopotential (temperature) fields so that the initial mass divergence tendency was zero.

60

Twelve-hour forecasts were then made with and without noise-freezing. The frozen forecast was made by subtracting 675 mb from the initial values of π while accounting for this change in the determination of the arrowed variables in (18)-(20). The frozen and unfrozen sea-level pressure forecasts are shown in Figs. 34 and 35, respectively, while Fig. 36 displays the verifying NMC analysis for 00Z 16 February 1976 (it should be noted that the sea-level pressure in Fig. 36 was also estimated from 1000 mb heights). The largest difference observed in Figs. 34 and 35 is the intensity of the high located at roughly 55°N, 40°E. Both forecasts are quite reasonable when compared to the NMC analysis in Fig. 36. Certainly the noise-freezing does not degrade the 12-hour forecast made by the model.

Next, the model was subjected to a large shock by reducing the temperatures at all three levels by 20°C at 33.75°N, 90°E. Frozen and unfrozen forecasts were run with and without this shock. Fig. 37 displays the difference field (shocked minus unshocked) for 1-hour unfrozen forecasts of π. The central value of the high exceeds 48 mb. The difference field for 3-hour frozen forecasts of π is shown in Fig. 38 where the central value of the high is just above 40 mb. It can be seen that noise-freezing has reduced the phase speed of the gravity waves by almost exactly a factor of three. In both figures a rather suspicious looking belt extends around the globe centered approximately at 45°N. This is the direct result of the Fourier filtering performed in the model poleward of 45°N. A similar plot for the 3-hour unfrozen forecasts
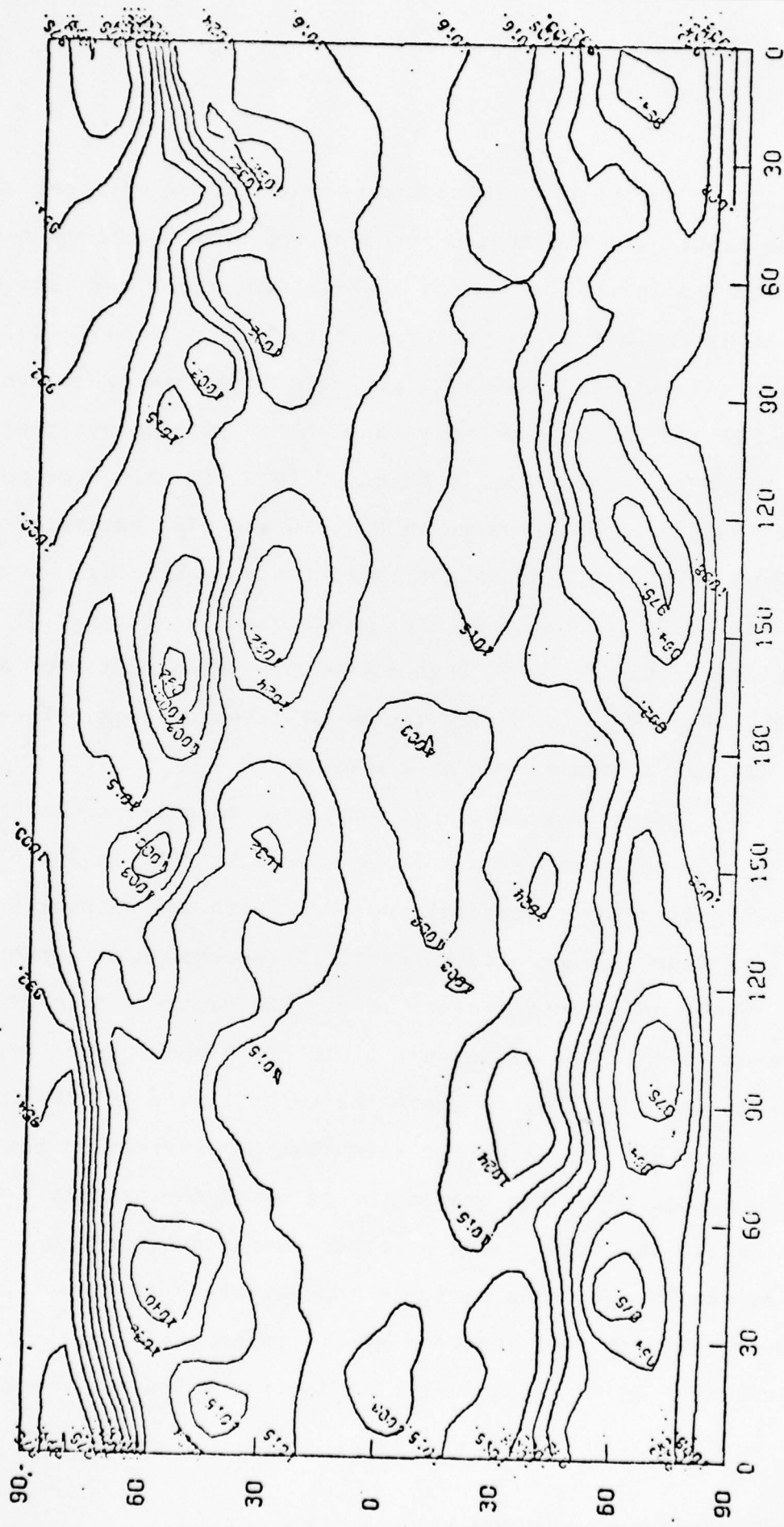
61

Fig. 34. Frozen 12-hour forecast sea-level pressure field (mb) valid at 00Z 16 February 1976.

Fig. 35. Unfrozen 12-hour forecast sea-level pressure field (mb) valid at 00Z 16 February 1976.

Fig. 36. NMC analysis sea-level pressure field (mb) for 00Z 16 February 1976.
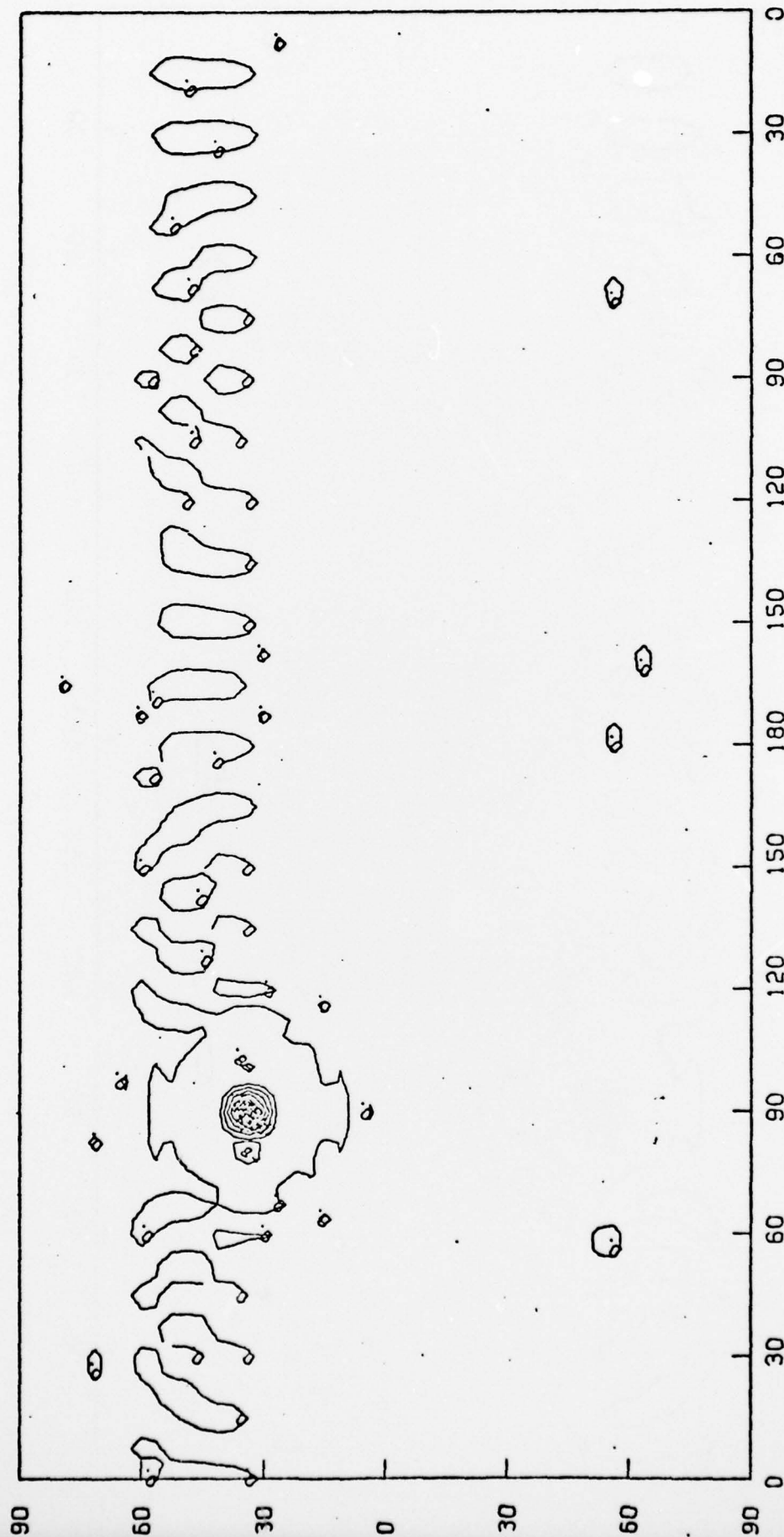
64

Fig. 37. Difference field (mb) between 1-hour unfrozen sea-level pressure forecasts (shocked minus unshocked) for 13Z 15 February 1976.
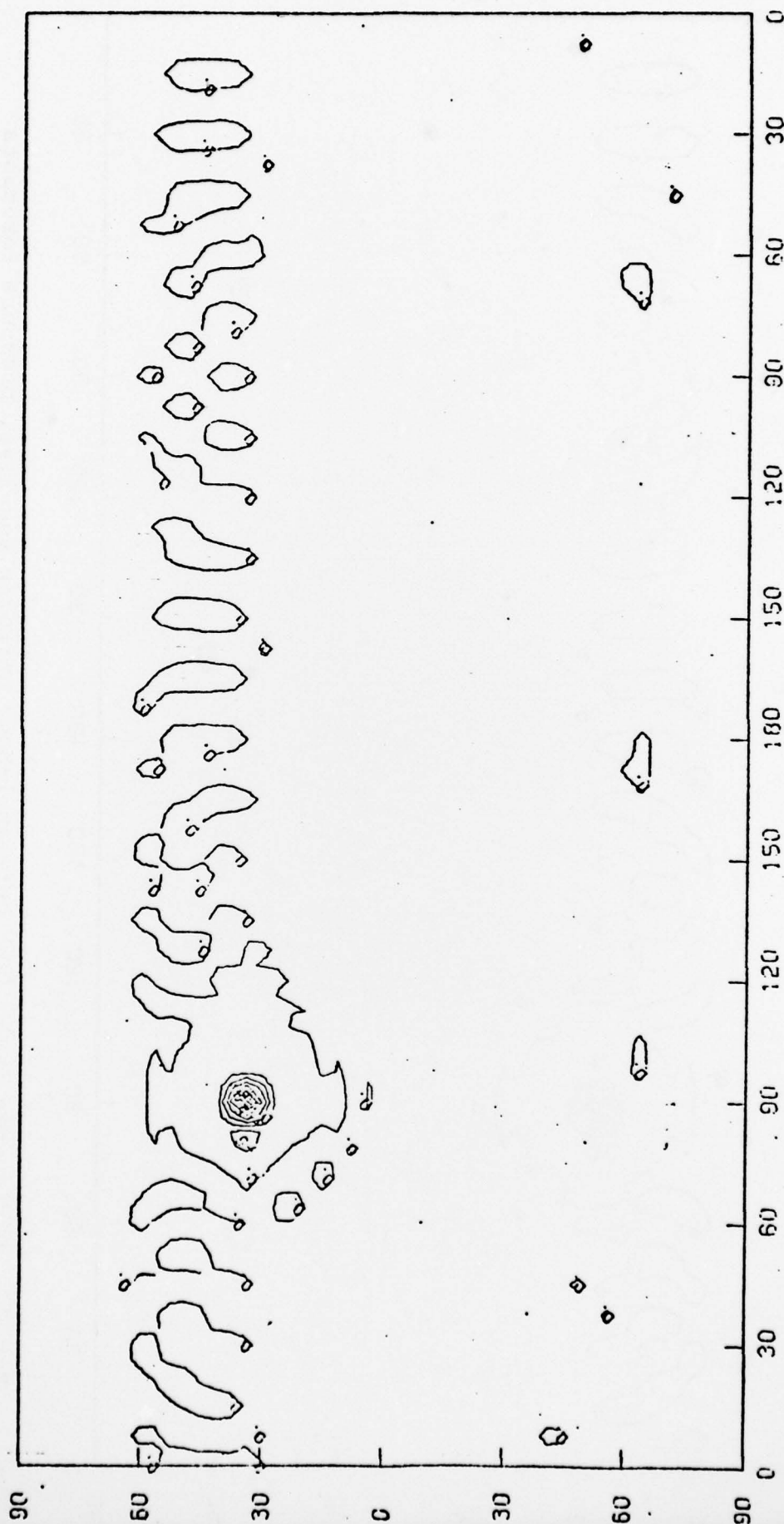
65

Fig. 38. Difference field (mb) between 3-hour frozen sea-level pressure forecasts (shocked minus unshocked) for 15Z 15 February 1976.

is displayed in Fig. 39 . It can be seen that the central value
of the high has diminished to about 24 mb and that the radius of
influence of the noise is roughly three times as large as that
in Figs. 4 and 5 . Thus, it can be seen in these figures that the
noise-freezing technique can be effectively applied to a baroclinic
primitive equation model in order to control the noise induced by
assimilation of satellite data into the model at asynoptic times.

Experiments are in progress to determine whether the
baroclinic assimilation model can produce initial fields which
result in an improved forecast. We are using the data which was
collected during Data Systems Tests 5 and 6 during the summer of
1975 and the winter of 1976. These data sets provide unprecedented
coverage of satellite and other asynoptic observations. Figure 40
depicts the global coverage by satellite soundings for a 12-hour
period. Figure 41 shows positions of satellite wind measurements
made by NMC. For these test periods a group at the University of
Wisconsin made wind measurements from satellite pictures using a
special technique. Their coverage is in figure 42 .

The wind data presents a special problem to the assimi-
lation scheme because all the measurements for the 12-hour period
were made at only two times.

Forecasts with and without the satellite soundings
shown in figure 40 were made for the 12-hour period. Figure 35
is the sea-level pressure forecast without assimilation. Figure
43 shows the assimilation forecast without the use of noise freez-
ing, and figure 44 is the equivalent forecast with the satellite
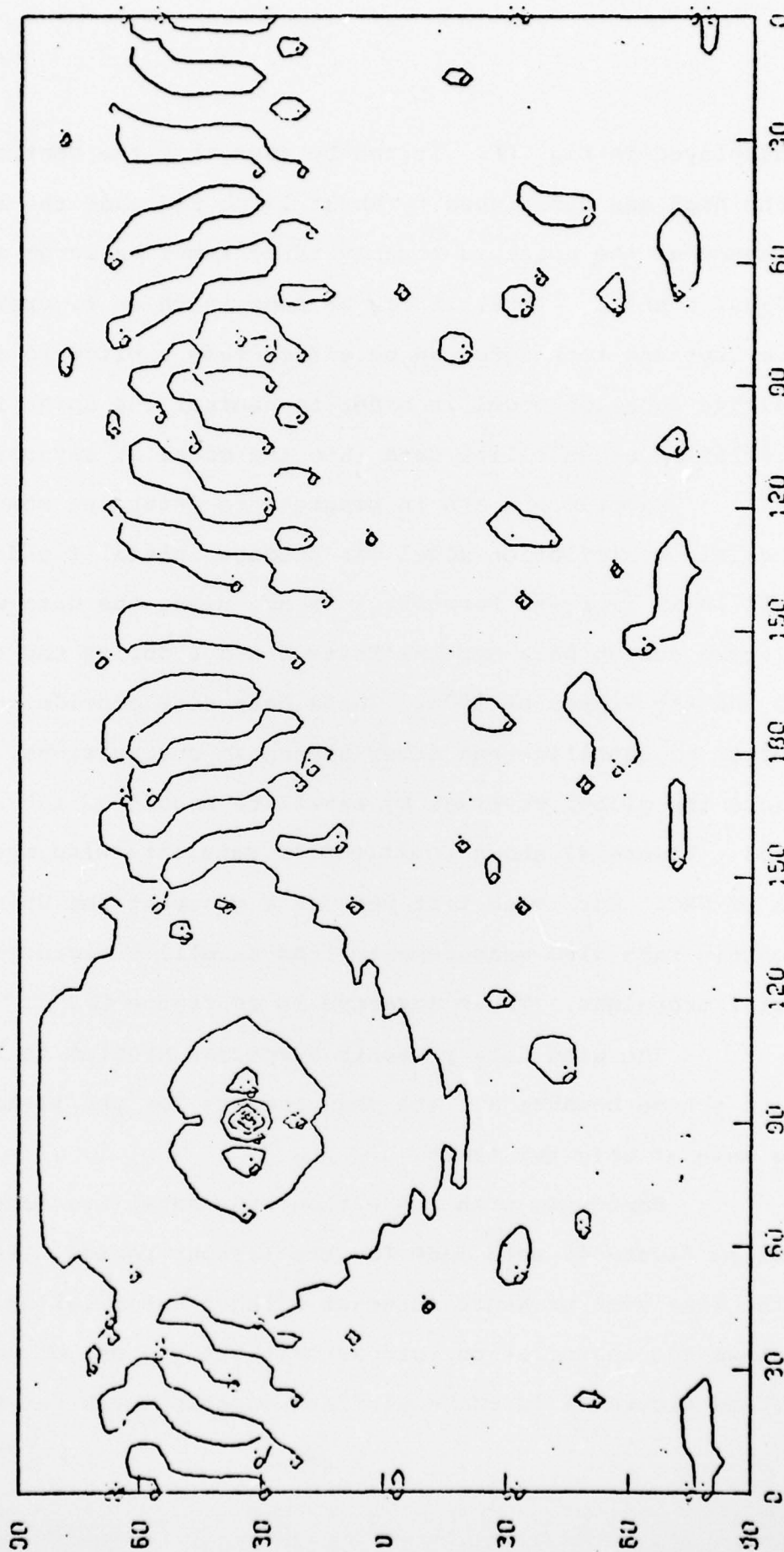
67

Fig. 39. Difference field (mb) between 3-hour unfrozen sea-level pressure forecasts (shocked minus unshocked) for 15Z 15 February 1976.
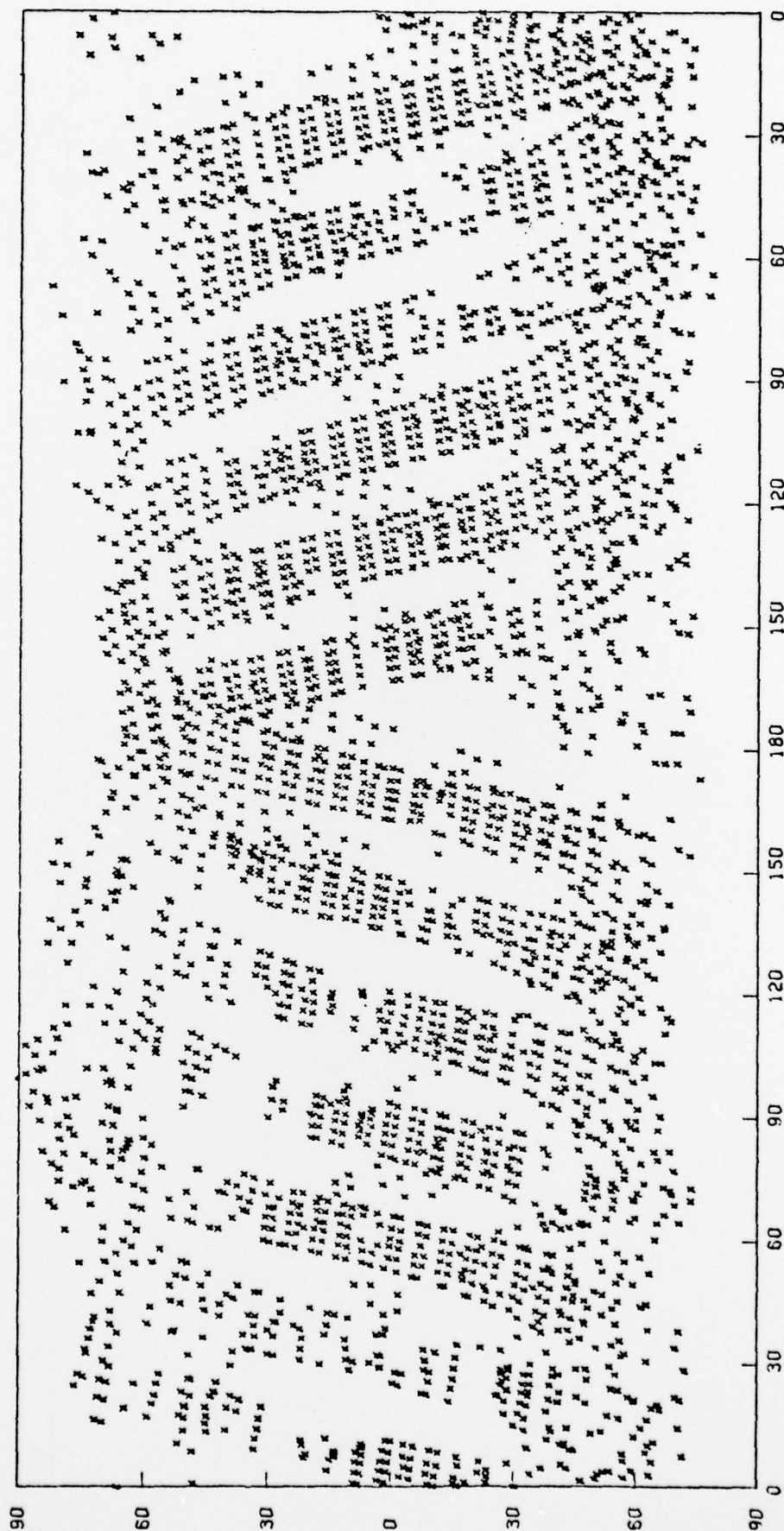
Fig. 40. Locations of SIRS and NIMBUS 6 Satellite Soundings for the 12-hour period 1200Z to 2400Z, 15 Feb., 1976.
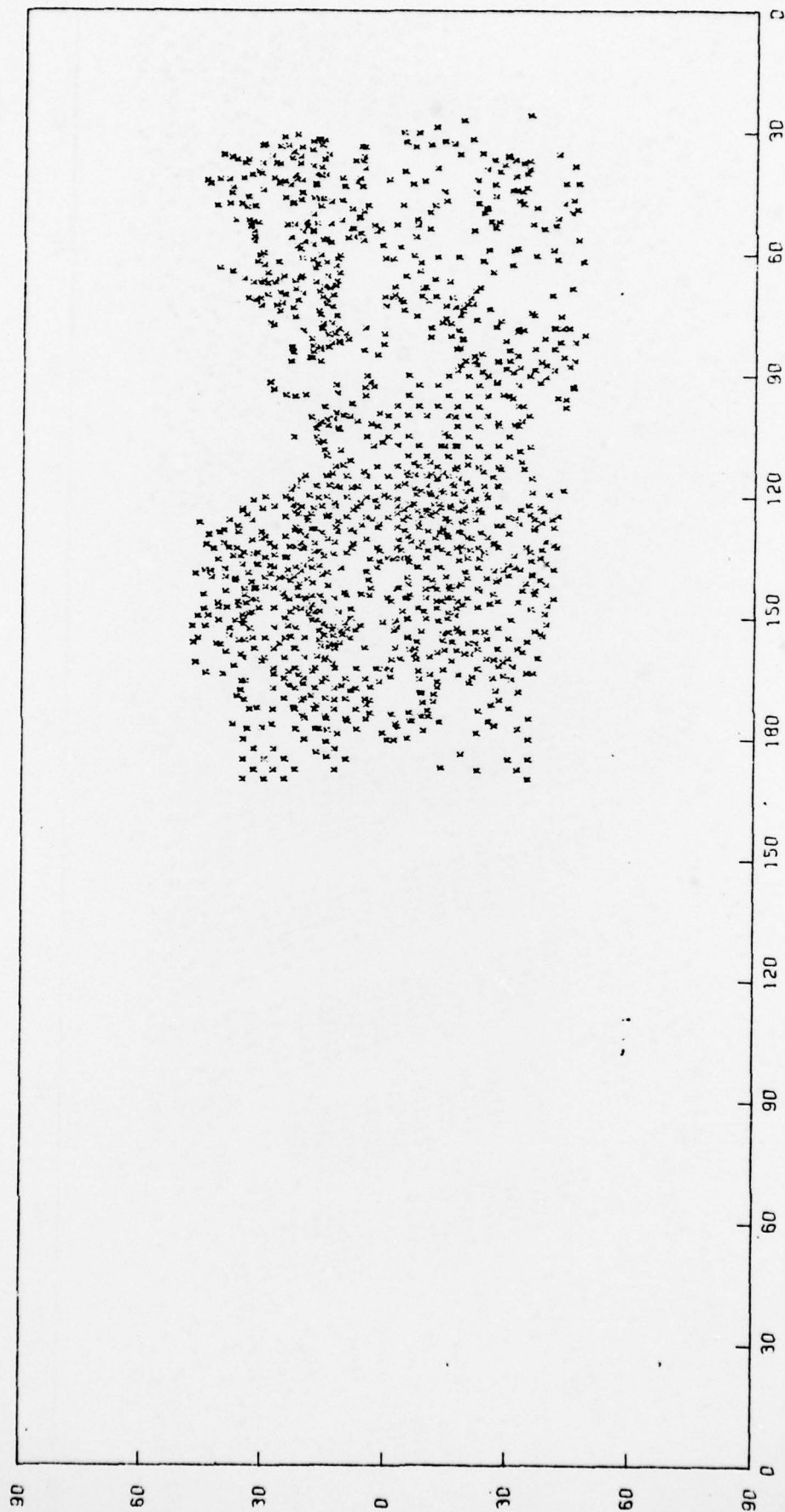
Fig. 41. Positions of NMC Satellite Wind Measurements for the 12-hour period 1200Z to 2400Z, 15 Feb., 1976.
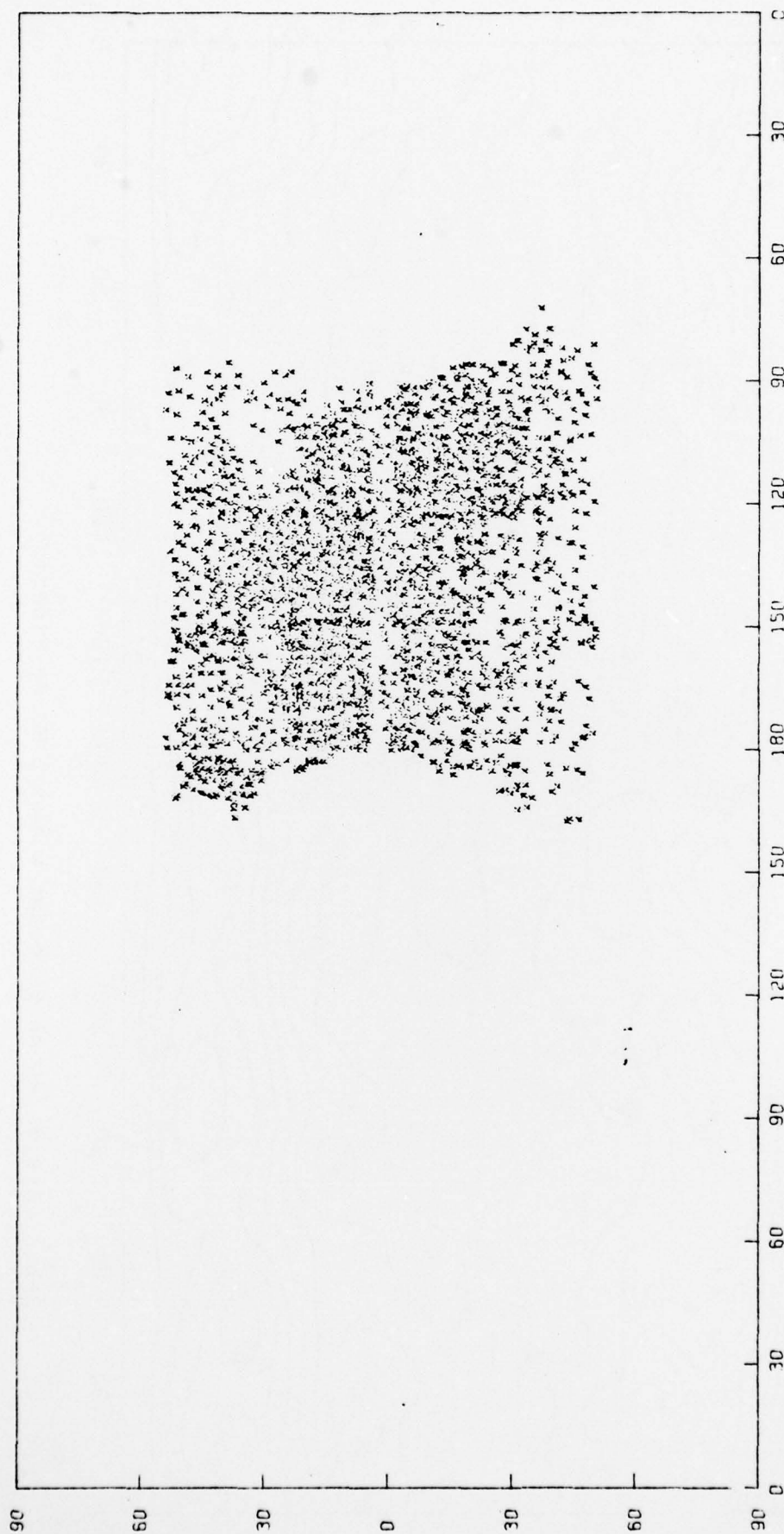
70

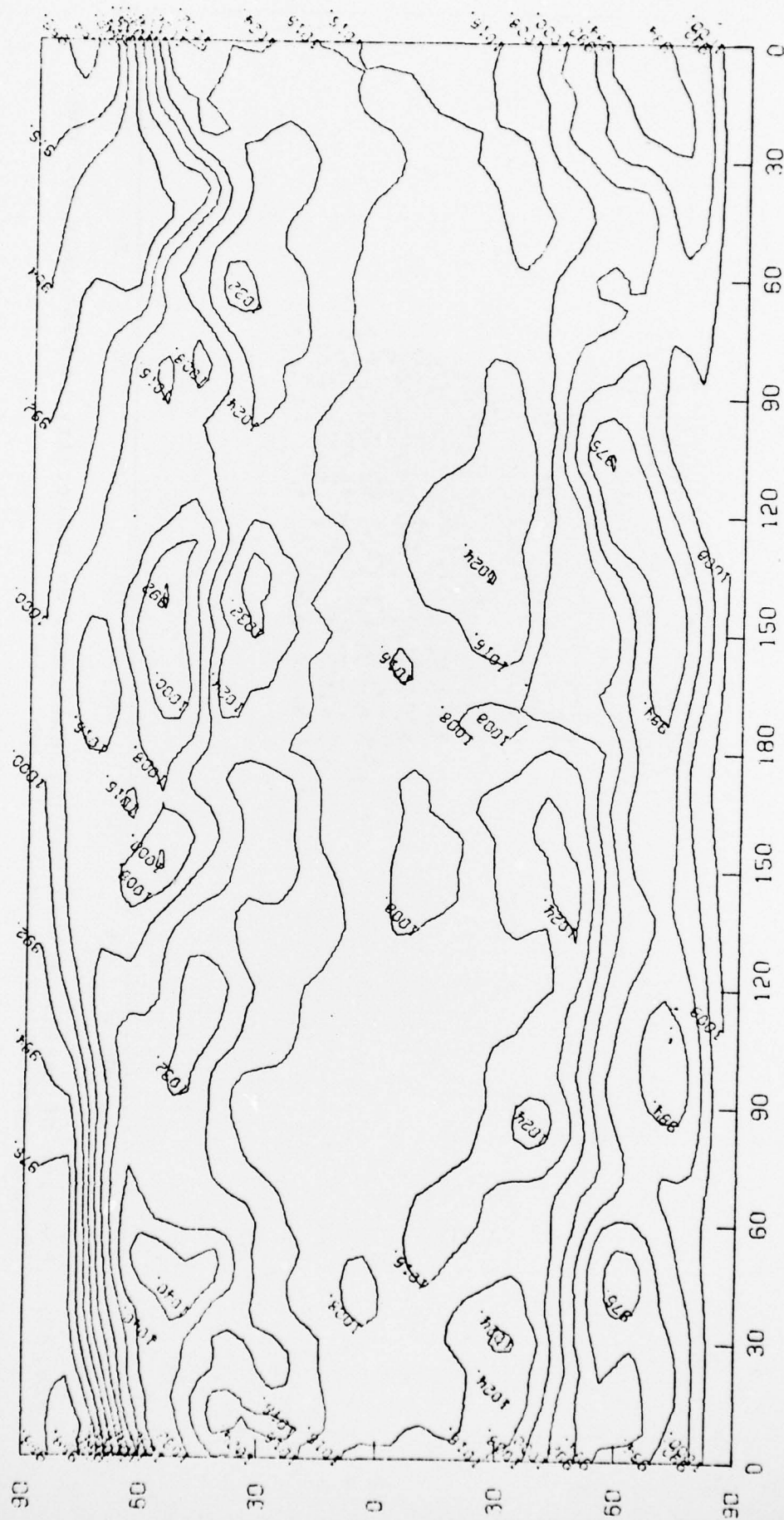Fig. 42. Position of Satellite Wind Measurements made by University of Wisconsin for the 12-hour period 1200Z to 2400Z, 15 Feb., 1976.

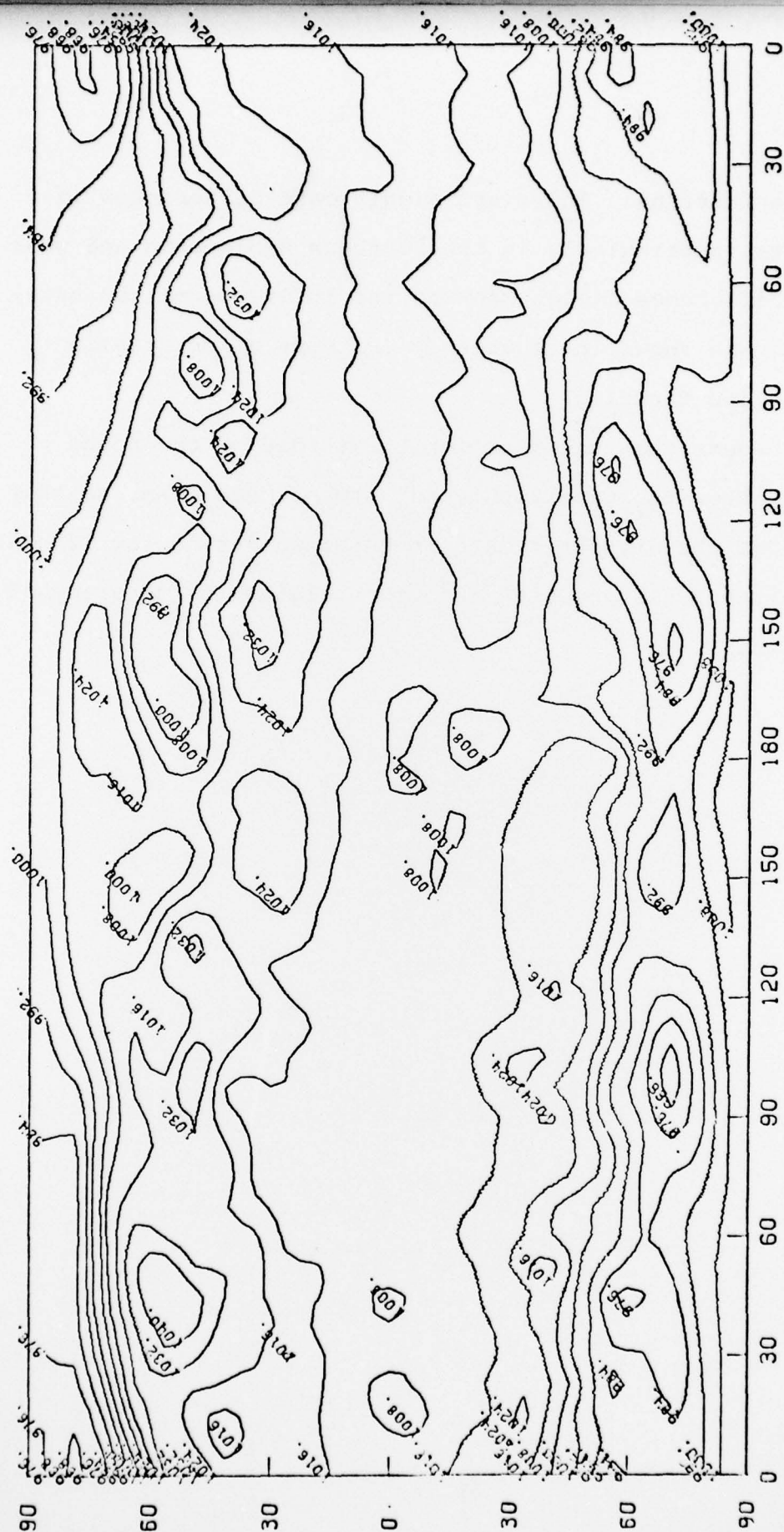Fig. 43. 12-hour Assimilation Forecast without Noise Freezing.

Fig. 44. 12-hour Assimilation Forecast with Noise Freezing.

73

data and noise freezing. There are significant differences in these forecasts, particularly in the Southern Hemisphere and near Alaska. The difference fields showing the influence of the satellite soundings are shown in figures 45 (without noise freezing) and 46 (with noise freezing).

It seems that the most important role of the noise freezing is to slow the geostrophic adjustment mechanism, so that the influence of the asynoptic data is retained during the 12-hour period. No attempt has yet been made to evaluate the accuracy of these forecasts.
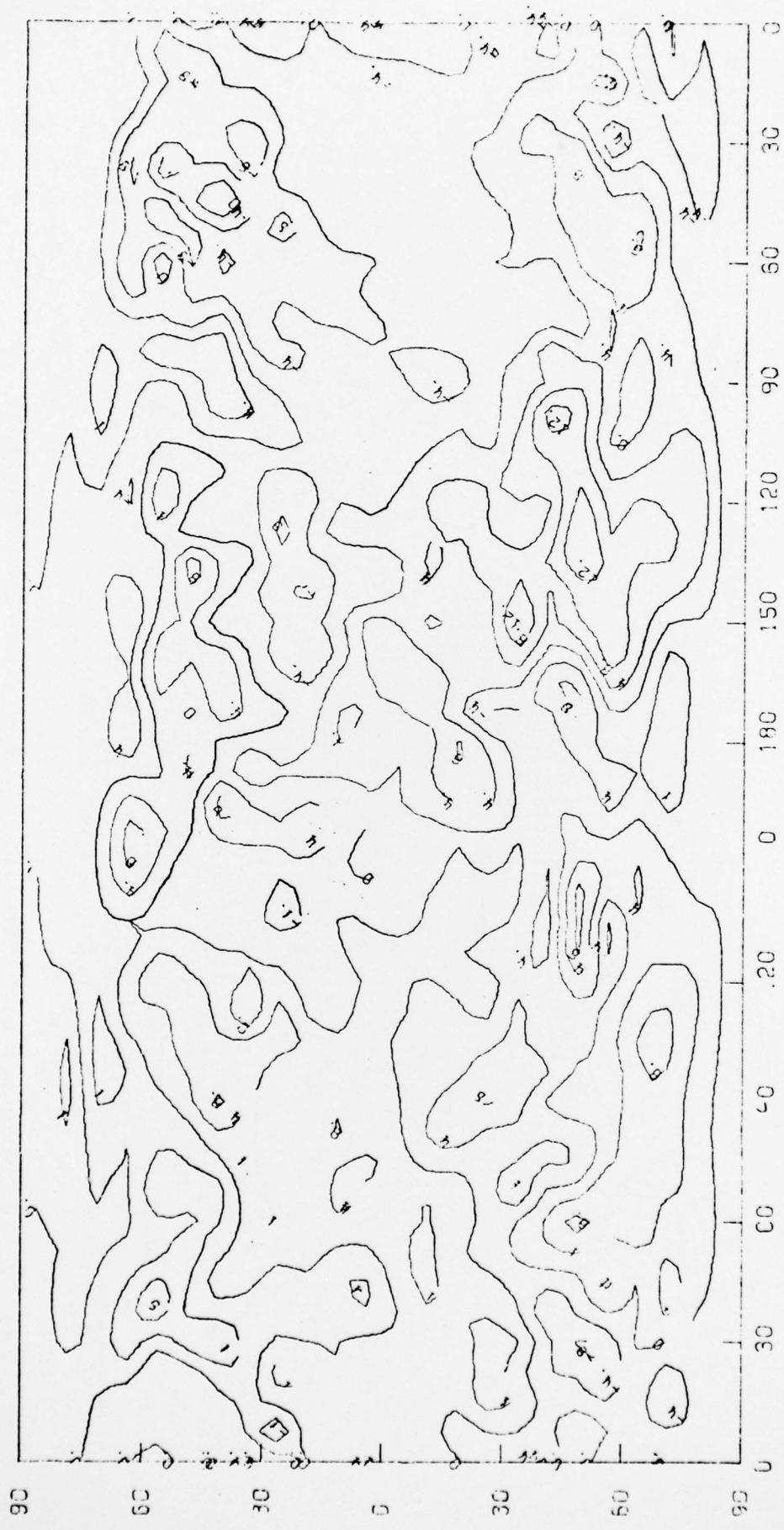
Fig. 45. 12-hour Forecast with Satellite Data - without Noise Freezing.
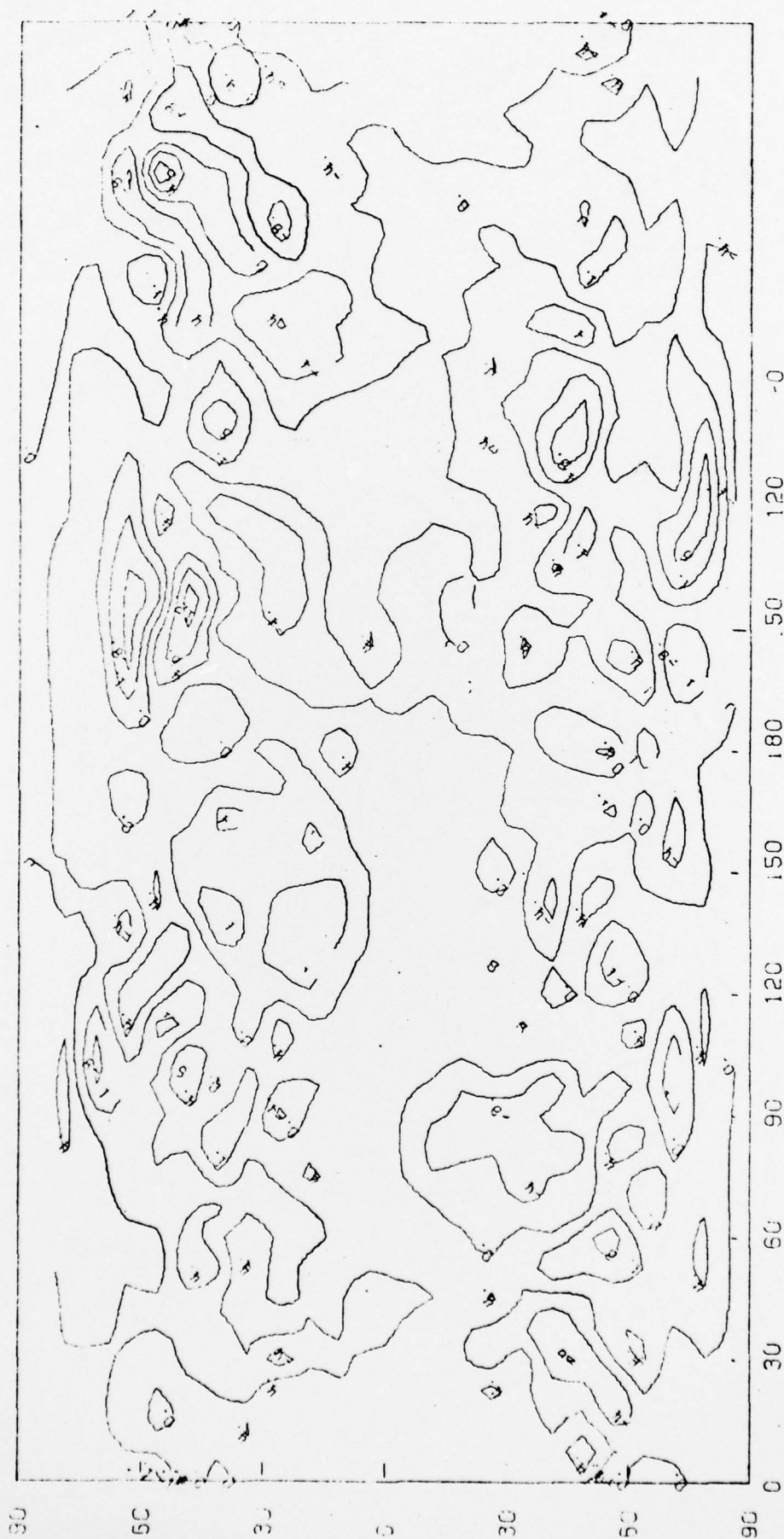
Fig. 46. 12-hour Forecast with Satellite Data - with Noise Freezing.

76

REFERENCES

Cressman, G., 1959: An operational objective analysis system. Mon. Wea. Rev., 87, 367-374.

Sasaki, Y.K., 1976a: Variational design of finite difference schemes for initial value problems with an integral invarient. J. Comp. Phys., 21, 3, 270-278.

_____, 1967b: An experiment of noise suppression in data assimilation: "noise freezing technique." Presented at JOC Study Group Conference on Data Assimilation, Paris, France, 17-21 November 1967.